Zero Field ESR of Magnetic Impurities in Superconductors: a Novel Technique for Measuring Magnetic Penetration Depth and Application to High T_c $YBa_2Cu_3O_{7-\delta}$

by

Tamar Pereg-Barnea

B.Sc., The Hebrew University, 1999

A THESIS SUBMITTED IN PARTIAL FULFILMENT OF
THE REQUIREMENTS FOR THE DEGREE OF

MASTER OF SCIENCE

in

THE FACULTY OF GRADUATE STUDIES

(Department of Physics and Astronomy)

We accept this thesis as conforming
to the required standard

THE UNIVERSITY OF BRITISH COLUMBIA

October 12, 2001

© Tamar Pereg-Barnea, 2001

In presenting this thesis in partial fulfilment of the requirements for an advanced degree at the University of British Columbia, I agree that the Library shall make it freely available for reference and study. I further agree that permission for extensive copying of this thesis for scholarly purposes may be granted by the head of my department or by his or her representatives. It is understood that copying or publication of this thesis for financial gain shall not be allowed without my written permission.

Department of Physics and Astronomy

The University Of British Columbia
Vancouver, Canada

Date October 12, 2001

Abstract

The Meissner effect in superconductors is characterized by an exponential decay of externally applied magnetic fields into the sample with a length scale λ, that is called the magnetic penetration depth. λ is directly related to the superfluid density of the superconductor and is therefore one of the most important probes of the intrinsic properties of superconductors. This work describes the development of a new technique for measuring the penetration depth at microwave frequencies and low temperatures. The surprising combination of two seemingly unrelated experiments has led to a direct method of measuring the magnetic penetration depth in the London limit of high T_c superconductors. Samples of high T_c YBCO with uniform doping of magnetic ions ($Gd_xY_{1-x}Ba_2Cu_3O_{7-\delta}$ where $x \approx 1.28\%$) were prepared. The magnetic ions embedded in the superconductor serve as magnetic field probes through a zero field Electron Spin Resonance (ESR) experiment. Measurement of the imaginary part of the magnetic susceptibility, $\chi''(\omega)$, through the sample's microwave surface resistance, reveals relatively sharp ESR transitions with integrated intensity that is proportional to the number of ions that are exposed to the field. With a uniform ion distribution, the number of ions that are exposed to the field is proportional to the penetration depth λ. The spectrum of $\chi''(\omega)$ is obtained from surface resistance measurement in a bolometric apparatus. Our new method was successfully applied to overdoped and optimally doped YBCO samples and absolute values of the a-b plane penetration depth at $T = 1.2$ are given.

Table of Contents

Abstract ii

Table of Contents iii

List of Tables v

List of Figures vi

Acknowledgments vii

Chapter 1: Introduction and Motivation 1

Chapter 2: Conductivity and Surface Impedance 4
2.1 The Two Fluid Model 4
2.2 Conductivity in the Two Fluid Model 4
2.3 Surface Impedance 5

Chapter 3: Penetration depth 9
3.1 Meissner effect and the London theory 9
3.2 London Penetration Depth 11
3.3 Magnetic Penetration Depth 12

Chapter 4: Electron Spin Resonance 14
4.1 Magnetic Resonance 14
4.2 Magnetic Ions in a Crystal: Fine Structure 16
4.3 Effective Spin Hamiltonian 17
4.3.1 Semi-Classical Approach for Deriving the Effective Spin Hamiltonian 18
4.4 Zero field ESR and the ESR Spectrum 20

Chapter 5: The Bolometric Experiment 23
5.1 The Measurement Principle 24

Chapter 6: λ Extraction Technique 27
6.1 The Samples 27
6.1.1 Sample Preparation 28
6.1.2 Gadolinium Concentration Determination 30
6.2 R_s and χ'' 31
6.3 Background Subtraction 32
6.4 Spectrum Fitting and Extraction of λ 32

Chapter 7: Results and Analysis **34**
7.1 Twinned Optimally Doped Crystal 34
7.1.1 Oxygen Ordering 37
7.2 Detwinned Overdoped Crystal 40
7.3 Corrections for $\hat{c}$ Axis Currents 42
7.4 Error analysis 45

Chapter 8: Conclusions **47**

References **49**

Appendix A: Cavity Perturbation Technique **53**

Appendix B: Surface Current in a Uniform magnetic Field **55**

List of Tables

7.1 Crystal field parameters for the two ESR bands in an optimally doped YBCO, given in GHz. 38
7.2 ESR Transitions in a twinned optimally doped YBCO sample. 40
7.3 Crystal field parameters for the ESR spectrum in an overdoped YBCO crystal, given in GHz. 42
7.4 ESR Transitions in a detwinned overdoped YBCO sample. 42
7.5 The ESR-extracted penetration depth λ of an optimally doped twinned sample and an overdoped detwinned sample, at $T = 1K$. Both samples have 1.28% Gd concentration. 44

List of Figures

2.1 A schematic picture of the complex conductivity of a superconductor as described by the two fluid model in different temperature regimes. 6

4.1 ESR transitions in a spin system. 15
4.2 ESR transitions at a constant frequency and varying DC magnetic field for a spin $\frac{3}{2}$ system. 21
4.3 Theoretical $\chi''(\omega)$ for a system with spin $\frac{7}{2}$ and fine structure Hamiltonian $\mathcal{H}_0 = B_2^0 O_2^0 = B_2^0(3S_z^2 - S^2)$. 22

5.1 The electromagnetic fields configuration in the bolometric apparatus. 25
5.2 A typical surface resistance spectrum of a YBCO sample at different temperatures as measured in the bolometric apparatus 26

6.1 The YBCO unit cell. 29

7.1 The surface resistance of a twinned optimally doped sample with 1.28% Gadolinium 35
7.2 The magnetic susceptibility χ'' of $Gd_{0.01}Y_{0.99}Ba_2Cu_3O_{6.92}$. 36
7.3 Two different crystal field environments. 37
7.4 The fitted ESR spectrum of an optimally doped YBCO sample with 1.28% Gd. 39
7.5 Surface resistance of an over doped YBCO sample with 1.28% Gd. . . 41
7.6 The fitted ESR spectrum of an over doped YBCO sample with 1.28% Gd. 43

B.1 A typical high T_c sample in a magnetic field 56

Acknowledgments

I would like to thank Dr. Walter Hardy for the great idea behind this work and for his guidance and support. It was a pleasure to work with and learn from Walter at all times.

Special thanks to Patrick Turner, who is my partner in this project, for his devotion to the work and for teaching me a great deal about bolometry and microwave techniques. This work has also benefitted from the help of Richard Harris who was always willing to discuss physics, consult and even wrote the first spectrum analysis Mathematica program.

The past year in the UBC superconductivity lab was challenging, interesting and very pleasant, thanks to everyone in the lab. I would like to thank Dr. Doug Bonn for co-supervision, Dr. Ruixing Liang for the high quality samples and chemical support and the other members of the group: Dr. David Broun, Pinder Dosanjh, Jennifer Babiak, Ahmad Hosseini, Saeid Kamal and Darren Peets who have contributed to this work directly and indirectly through discussions, editorial assistance or simply by making it fun to be a part of the group.

We have also received help from Dr. Andras Janossy whose previous study of Gd doped YBCO was the basis of this work and the correspondence with him, in person, was enlightening.

Eventually I would like to thank my family for their support and my dear husband, Amir, for being a source of comfort and inspiration.

1: Introduction and Motivation

Since 1986, when Bednorz and Müller first discovered high temperature superconductivity in $La_{1.85}Ba_{0.15}CuO_4$, the topic of high T_c superconductivity has remained one the most interesting open questions of condensed matter physics. High T_c superconductors are not only superconducting at temperatures much higher than the boiling temperature of nitrogen, which opens up the possibility of many new applications, but they are also very different from the well known "conventional" superconductors. While previously existing superconductors were well understood by the BCS theory which is based on a phonon mediated s-wave pairing mechanism [1], the high T_c superconductors show many deviations from this behavior.

The London penetration depth, λ_L, provides also colloquial useful information about the nature of the superconductor. It will be shown in chapter 3 that $1/\lambda_L^2 \propto n_s/m^*$ where n_s is the density of the supercurrent carriers (the supercarriers) and m^* is their effective mass. This result motivates the study of the penetration depth, since λ_L and its temperature dependence provides access to two of the superconductor's intrinsic properties, the supercarrier density and the energy spectrum of the quasiparticle excitations.

It is well established that except in special cases, superconductors have an energy gap, Δ, in their density of states spectrum. This can be seen, for example, in STM experiments. In the language of the BCS theory, superconductivity is the result of pairing between electrons (Cooper pairs). The gap energy is a measure of the energy required to break a pair. At low temperatures, the system is condensed in its paired ground state (also called the condensate) and excitation cannot be created by collisions. This leads to frictionless motion of the condensate. However, the shape of the gap in k-space, $\Delta(\vec{k})$, may vary from one material to another. One of the main differences between the high T_c and the conventional superconductors is the symmetry of the superconduction gap. A conventional superconductor has an s-wave gap symmetry, meaning that Δ is the same in every direction: $\Delta(\vec{k}) = \Delta_0$. More generally, an s-wave gap is often taken to be any dependence $\Delta(k)$ that has the full symmetry of the lattice. The high T_c superconductors were found to have a d-wave gap symmetry: $\Delta \propto k_x^2 - k_y^2$. This fact is reflected in many of their temperature dependent properties. Some of the first evidence for the d-wave pairing symmetry was observed

by Hardy *et al.* at UBC [?], where measurements of $\lambda(T)$ at microwave frequencies showed a linear temperature dependence. The linear temperature dependence of λ indicated a node in the gap function, a direction in which the gap is zero. Although nodes can exist in a gap with anisotropic s-wave symmetry, it is rather unlikely. In addition, measurements sensitive to the phase of the gap confirm that indeed the gap has predominantly d-wave symmetry.

Another interesting feature of the high T_c superconductors is their quasi two dimensional structure where most of the conduction takes place in the copper-oxygen (CuO_2) planes. The carriers in the planes are believed to be holes rather than electrons and the number of holes per unit cell, x, is controlled by the structure of the material outside the Cu-O planes. For example, in YBCO, where the O_3 sites form chains in the $\hat{b}$ direction, the overall oxygen content determines the average chain length which in turn affects the number of supercarriers in the planes. In 1989, Uemura *et al.* demonstrated a universal relation between the superfluid density, n_s, and T_c. It was found, in several high T_c superconductors and for a range of doping levels, that T_c varies linearly with n_s up to a certain optimal density at which T_c saturates and then is suppressed [3]. These results were obtained through muon spin rotation (μSR) experiments, where the muon spin relaxation rate, σ, which is proportional to $1/\lambda^2$, was measured. Its limit at zero temperature, $\sigma(T \to 0)$, is proportional to the carrier density at zero temperature and a sharp drop in $\sigma(T)$ indicates T_c. This universal doping dependence of T_c reflects certain intrinsic properties of the Cu-O planes.

In the last decade a considerable amount of effort has gone towards measuring microwave properties of the Hi T_c superconductors. A wide variety of microwave data is available on both the real part of the conductivity and the London penetration depth at different frequencies and temperatures (see for example [4, 5, 6]). However, the limit as $T \to 0$ is still not well tested. In particular, an absolute measure of $\lambda_L(T)$ is challenging to measure. Any volume exclusion technique that aims to measure λ_L to within 10% would require an accurate measurement of the sample thickness to better than 1/1000 and very precise control of demagnetization effects (see [7] for more details).

In our lab, $\Delta\lambda_L(T)$ of high purity $YBa_2Cu_3O_{7-\delta}$ (YBCO) is measured through a cavity perturbation method that is described in appendix A. The difficulty of measuring the sample thickness restricts the penetration depth to be measured only up to an additive constant, i.e the temperature dependence $\Delta\lambda_L(T) = \lambda_L(T) - \lambda_L(T_{base})$ is resolved, but an absolute value of $\lambda_L(T_{base})$ cannot be obtained. Therefore some

other method is required. Moreover, one cannot extract the complex conductivity $\sigma(\omega, T)$ from the surface impedance without knowing $\lambda_L(T_{base})$. In order to complete the data, a value of $\lambda(T = 0)$ is inferred either from μSR experiments [8, 9] or from infrared reflection [10]. Values obtained from far infrared spectroscopy, for example, are $\lambda_a = 1600\mathring{A}$ and $\lambda_b = 1000\mathring{A}$ for $YBa_2Cu_3O_{6.95}$. However, the infrared spectroscopy method is extremely demanding and cannot practically be used for a variety of samples.

It should be mentioned that μSR experiments determine λ in the vortex state as the length scale over which the magnetic field decays from the normal core to the superconducting bulk. It is now known that the effective λ is field dependent, which is interesting in itself, but this means that the μSR values do not correspond directly to the Meissner state λ. In addition μSR measurements are limited to a geometrical average between λ_a and λ_b. On the other hand, extracting λ from infrared reflection involves performing a type of Kramers Kronig integral of the data from zero to infinity frequency. In practice, the measurements exist only over a finite range of frequencies and some extrapolation is required. This extrapolation reduces the accuracy and sometimes underestimates the importance of low frequency spectral weight.

The purpose of the new technique described here is to provide an absolute measurement of $\lambda_L(T_{base})$ at a low base temperature. This method involves preparing a superconducting sample (YBCO) that is doped with magnetic ions (Gadolinium) and therefore cannot be applied to existing samples. However, we assume that the doped samples have the same penetration depth as undoped YBCO crystals with the same oxygen concentration. This assumption is based on the low concentration of Gd ions in the sample and on the detailed chemistry of Gd substitution in YBCO. In particular the Gadolinium substitutes only for Yttrium, has the same charge and is located at a symmetric position between the CuO_2 planes and not on the planes. Finally, because the lattice parameters and T_c for $GdBa_2Cu_3O_{7-\delta}$ are known and not very different from YBCO ($a = 3.92\mathring{A}$, $b = 3.85\mathring{A}$, $c = 11.75\mathring{A}$ and $T_c = 94K$ [?]), it is clear that Gd is a rather weak perturbation on YBCO.

This thesis contains some introductory material on superconductivity, microwave spectroscopy and ESR experiments (chapters 2 - 4), description of the new method and its application to YBCO (chapters 5 and 6), and finally the results are given and discussed in chapters 7 and 8.

2: Conductivity and Surface Impedance

The theory of high T_c superconductors is yet to be established. Nevertheless, some simple phenomenological descriptions of superconductivity are available and can be applied to high T_c materials.

2.1 The Two Fluid Model

The two fluid model of F. and H. London provides a basic picture of superconductivity without assuming a specific mechanism that leads to superconductivity. Any theory of the mechanism (such as the BCS theory) can be combined with this model to complete the picture. The two fluid model divides the charge carriers (originally thought of as electrons) into two groups. One group contains the normal carriers which do not take part in the superconductivity. The other component, called the superfluid, contains the supercarriers, gapped excitations (cooper pairs in the BCS language) that condense below T_c and exhibit frictionless motion. The supercarriers, also referred to as the condensate, are responsible for the superconductivity while the normal carriers exhibit scattering processes. The two groups may exchange particles as long as the total spectral weight ne^2/m^* (where n is the carrier density and m^* is the effective mass) is conserved.

We shall follow the description of this model by Tinkham [11]. Let us denote the fraction of carriers that are normal by x and the fractional number of supercarriers by $(1-x)$, so that the total number of carriers is conserved. The normal fraction varies with temperature with $x \to 1$ above T_c and $x \to 0$ at $T \to 0$.

2.2 Conductivity in the Two Fluid Model

Within the framework of the two fluid model, let us use the simplest transport picture, the classical Drude model. In the Drude model under the influence of an applied electric field $\vec{E}$, the charge carriers travel uninterrupted for an average time τ. The free motion ends when a collision of an unspecified nature occurs and the carrier is scatted. The equation of motion of a charge carrier with effective mass m^* and charge

$-e$ is:

$$m^*\ddot{r} + \frac{m^*\dot{r}}{\tau} = -eE. \tag{2.1}$$

Assuming an AC field with angular frequency ω and time dependence of $e^{i\omega t}$ leads to a complex conductivity σ that is defined as $\vec{J} = \sigma\vec{E}$ and is given by:

$$\sigma(\omega) = \sigma_1 - i\sigma_2 = \frac{ne^2\tau/m^*}{1+i\omega\tau} = \frac{ne^2\tau/m^*}{1+\omega^2\tau^2}(1-i\omega\tau) \tag{2.2}$$

where n is the total number of carriers. In a normal metal at microwave frequencies and below, $\omega\tau \ll 1$ and σ is effectively real: $\sigma \approx \sigma_1 = \frac{ne^2\tau}{m}$. A simple picture of a superconductor is obtained by taking the limit $\tau \to \infty$. In this case, the conductivity away from $\omega = 0$ is primarily imaginary and the real part σ_1 shrinks to a delta function at zero frequency.

$$\sigma_s(\omega) = \frac{n_s e^2}{m^*}\pi\delta(\omega) - i\frac{n_s e^2}{m^*\omega} \tag{2.3}$$

where n becomes n_s, the number of supercarriers. In the presence of both super and normal fluids the conductivity is the following sum:

$$\sigma = \sigma_s + \sigma_n = \sigma_1 - i\sigma_2 \tag{2.4}$$

$$\sigma_1(\omega) = \frac{n_s e^2}{m^*}\pi\delta(\omega) + \frac{n_n e^2}{m^*}\frac{\tau}{1+\omega^2\tau^2} \tag{2.5}$$

$$\sigma_2(\omega) = \frac{n_s e^2}{m^*\omega} + \frac{n_n e^2}{m^*}\frac{\omega\tau^2}{1+\omega^2\tau^2}. \tag{2.6}$$

Using (for example) the phenomenological Gorter/Casimir T dependence of x: $x = (\frac{T}{T_c})^4$, leads to negligible contribution of normal carriers to the conductivity at $T \approx 0.2T_c$. Therefore at any finite low frequency, $\sigma \approx -i\sigma_2$. Figure 2.1 shows σ_1 and σ_2, schematically, at different temperatures.

2.3 Surface Impedance

Microwave properties of superconductors such as the surface impedance can shed useful light on the intrinsic properties of a superconducting sample. Given that the shielding currents are confined to a very thin surface region, it is convenient to introduce the surface impedance, Z_s. It is defined by the ratio between tangential magnetic and electric fields at the sample's surface and can be measured in microwave cavities (see for example [4, 5, 6, 12]). When the magnetic field is applied in the $\hat{x}$

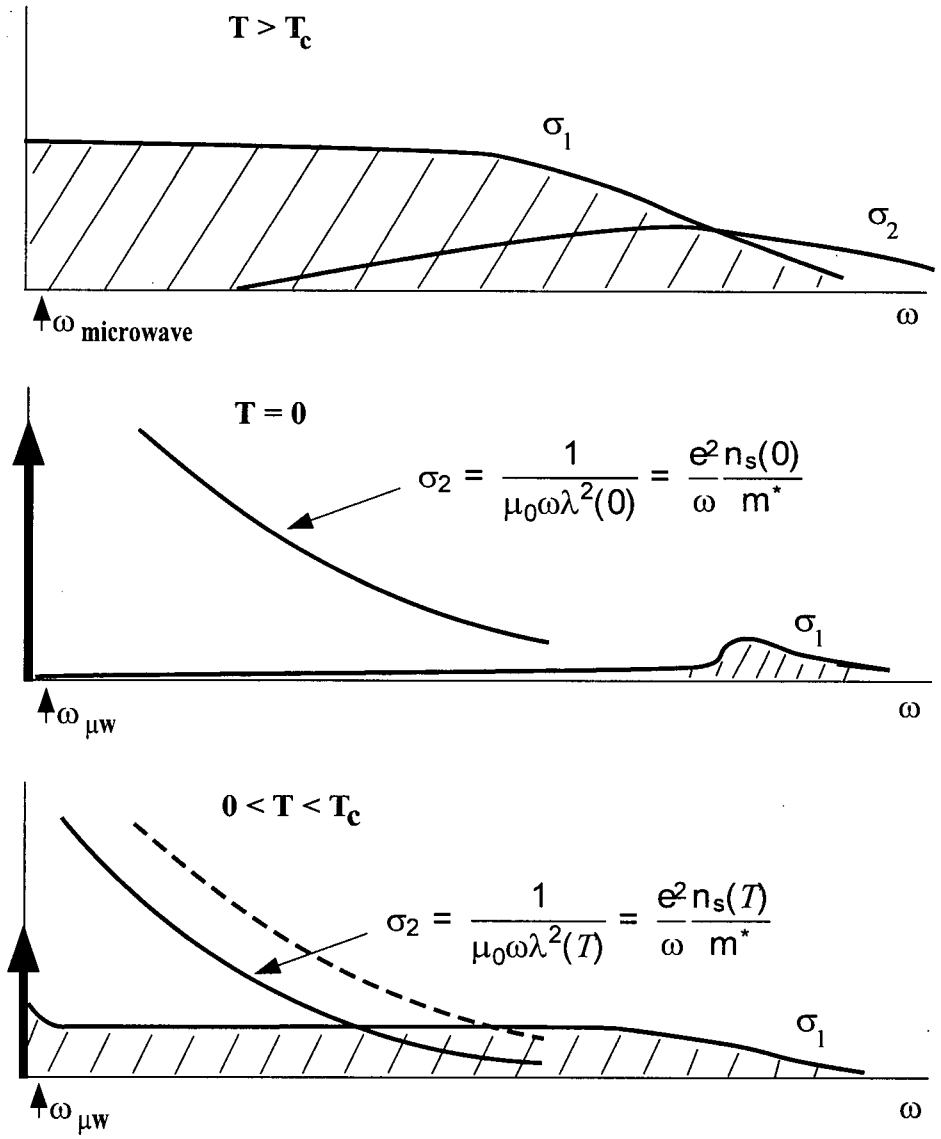

Figure 2.1: A schematic picture of the complex conductivity of a superconductor as described by the two fluid model in different temperature regimes. The upper figure shows the normal limit where the lifetime τ is finite and $\sigma = \frac{ne^2\tau/m}{1+i\omega\tau} = \frac{ne^2\tau/m}{1+\omega^2\tau^2}(1-i\omega\tau)$. The middle figure shows the $T \to 0$ limit where the real part shrinks to a δ-function around $\omega = 0$ and the imaginary part is proportional to $\frac{1}{\omega}$. The small peak in σ_1 at high frequency corresponds to excitations above the gap. The bottom figure shows an intermediate temperature, in the superconducting state.

direction, the electric field is induced in the $\hat{y}$ direction. The surface impedance is defined as:

$$Z_s = \frac{E_y}{H_x} = R_s + iX_s \tag{2.7}$$

where R_s is called the surface resistance and X_s is the surface reactance. The relation between Z_s and the conductivity σ can be found through the following classical skin effect calculation ([13]).

Consider a semi-infinite conductor (or superconductor) in the $Z > 0$ space with uniform complex conductivity σ. An oscillatory external magnetic field that is uniform in the x-y plane and varies in time is applied in the $\hat{x}$ direction: $\vec{H}(\vec{r},t) = H_x(z)e^{-i\omega t}$ where taking the real part to obtain the physical field is implicit. The electromagnetic fields will obey Maxwell's equations and Ohm's law:

$$\vec{\nabla} \times \vec{H} = \vec{J}, \qquad \vec{\nabla} \cdot \vec{B} = 0, \qquad \vec{\nabla} \times \vec{E} + \frac{\partial \vec{B}}{\partial t} = 0, \qquad \vec{J} = \sigma \vec{E}. \tag{2.8}$$

Since $\vec{H}$ is applied in the $\hat{x}$ direction its solution for the equations above varies only in the $\hat{z}$ direction. Expressing the above equations in terms of the magnetic field, H, and taking

$$\vec{\nabla} \times \vec{\nabla} \times \vec{H} = -\frac{\partial^2 H_x}{\partial z^2} \quad \text{and} \quad \frac{\partial H_x}{\partial t} = -i\omega H_x \tag{2.9}$$

yields:

$$(\frac{d^2}{dz^2} + i\mu_0\sigma\omega)H_x(z) = 0 \tag{2.10}$$

with general solution $H_x(z) = H_{x0}e^{ikz}$ where $k^2 = i\mu_0\sigma\omega$. In a normal metal, at microwave frequencies, σ is effectively real so that $k = (1+i)\sqrt{\frac{\mu_0\sigma\omega}{2}}$ and

$$H_x(z) = H_{x0}e^{i\frac{z}{\delta} - \frac{z}{\delta}}. \tag{2.11}$$

where δ is the classical skin depth: $\delta = \sqrt{\frac{2}{\mu_0\sigma\omega}}$. However, this is not the case in a superconductor where σ is primarily imaginary for low frequencies. If we assume $\sigma = -i\sigma_2$ then $k^2 = \mu_0\sigma_2\omega$ and the field decays as $H_{x0}\exp(-\frac{z}{\lambda})$ with the penetration depth:

$$\lambda = \sqrt{\frac{1}{\mu_0\sigma_2\omega}}. \tag{2.12}$$

The electric field $\vec{E}$ obeys the same equation as $\vec{H}$ in the $\hat{y}$ direction and therefore has the same spatial decay. Eliminating the exponents, the equation for $\vec{\nabla} \times \vec{E}$ is

reduced to:

$$-\frac{dE_y}{dz} = -\mu_0 \frac{dH_x}{dt} \Rightarrow ikE_y = -i\mu_0\omega H_x \tag{2.13}$$

and the surface impedance follows:

$$Z_s = \frac{E_y(z=0)}{H_x} = \frac{-i\mu_0\omega}{k} = \sqrt{\frac{i\mu_0\omega}{\sigma}}. \tag{2.14}$$

In general the conductivity is complex: $\sigma = \sigma_1 - i\sigma_2$ and we obtain

$$R_s = \sqrt{\frac{\mu_0\omega(\sqrt{\sigma_1^2+\sigma_2^2}-\sigma_2)}{2(\sigma_1^2+\sigma_2^2)}} \qquad X_s = \sqrt{\frac{\mu_0\omega(\sqrt{\sigma_1^2+\sigma_2^2}+\sigma_2)}{2(\sigma_1^2+\sigma_2^2)}} \tag{2.15}$$

In the normal state $\sigma_1 \gg \sigma_2$ and therefore $R_s = X_s = \sqrt{\frac{\mu_0\omega}{2\sigma}}$. In the superconducting state at low frequency σ_2 becomes much larger than σ_1 as soon as T drops below T_c and the surface resistance and reactance reduce to:

$$R_s = \frac{1}{2}\sqrt{\frac{\mu_0\omega\sigma_1^2}{\sigma_2^3}} \tag{2.16}$$

$$X_s = \sqrt{\frac{\mu_0\omega}{\sigma_2}}. \tag{2.17}$$

Combining this result with our definition of the penetration depth $\sigma_2 = 1/\lambda^2\omega\mu_0$ gives the relation between the surface impedance and λ and σ_1:

$$R_s = \frac{1}{2}\sqrt{\frac{\mu_0\omega\sigma_1^2}{\sigma_2^3}} = \frac{1}{2}\mu_0^2\omega^2\lambda^3\sigma_1 \qquad X_s = \sqrt{\frac{\mu_0\omega}{\sigma_2}} = \mu_0\omega\lambda. \tag{2.18}$$

Microwave techniques that measure surface reactance give direct access to the penetration depth and therefore to the superfluid density, as we shall see later on. Measurements of the surface resistance (combined with λ) can give the real part of the conductivity σ_1.

3: Penetration depth

The magnetic penetration depth has been introduced in the previous chapter as the skin depth of a superconductor in a time varying magnetic field. In this chapter we show that the exponential decay of magnetic fields (constant or time dependent) is closely related to superconductivity. In particular, the decay constant, λ is closely related to the superfluid density.

3.1 Meissner effect and the London theory

The Meissner effect in conventional superconductors was first observed experimentally by Meissner and Ochsenfeld, in 1933. In 1935 F. & H. London showed that the phenomena of superconductivity is closely related to near-perfect diamagnetism and explained the Meissner effect theoretically. In the Meissner effect, the superconductor expels any applied magnetic field from its volume through a shielding supercurrent traversing its surface. Type I superconductors (such as many elemental superconductors) are materials that have only two phases separated by a critical field H_c. The normal state, above H_c, in which the magnetic field fully penetrates the sample and the Meissner state where effectively no field penetrates the sample. Type II superconductors (for example many conventional alloy superconductors and the high T_c materials) are materials in which a so called vortex state exists. In these materials, below the critical field H_{c1} the sample is in the Meissner state and above a higher critical field H_{c2} the material is normal. In the region between H_{c1} and H_{c2} there is a vortex state in which the field penetrates the sample in the form of vortices. In this state the bulk superconductivity isn't destroyed and the vortices can form a two dimensional lattice. The London theory describes type I superconductors in a magnetic field below H_c or a type II superconductors in magnetic fields smaller than H_{c1}.

The theory begins with minimizing the free energy of a superconducting sample in an applied magnetic field. We assume that the thermodynamic state that minimizes the free energy includes a steady surface current. The free energy is:

$$\mathcal{F} = \int F_s d\vec{r} + E_{kin} + E_{magnetic} \tag{3.1}$$

where F_s is the free energy of the charge carriers in the superconducting condensate [14], E_{kin} is their kinetic energy associated with the constant current and $E_{magnetic}$ depends on the magnetic field configuration. Let us define $\vec{v}(\vec{r})$ to be the velocity of the charge carriers and j_s the resulting supercurrent as: $\vec{j}_s(\vec{r}) = n_s e\vec{v}(\vec{r})$ where n_s is the density of the carriers in the condensate and $\vec{v}(\vec{r})$ is their velocity. The constant flow of currents results in a kinetic energy of:

$$E_{kin} = \int \frac{1}{2} m v^2 n_s d\vec{r} \tag{3.2}$$

and the vector $\vec{r}$ spans the sample volume. The magnetic energy is given by:

$$E_{magnetic} = \frac{1}{2\mu_0} \int \vec{B}^2 d\vec{r}. \tag{3.3}$$

The relation between the current j_s and the magnetic field H is given by Maxwells equation:

$$\vec{\nabla} \times \vec{H} = \frac{1}{\mu_0} \vec{\nabla} \times \vec{B} = \vec{J}_s. \tag{3.4}$$

The total free energy is then:

$$\mathcal{F} = \int F_s d\vec{r} + \frac{1}{2\mu_0} \int [B^2 + \lambda_L^2 |\vec{\nabla} \times \vec{B}|^2] d\vec{r} \tag{3.5}$$

where the constant λ_L is defined by

$$\lambda_L = [\frac{m}{n_s e^2 \mu_0}]^{1/2}. \tag{3.6}$$

Minimizing the free energy with respect to the magnetic field $\vec{B}$ will determine the field configuration inside the sample. To minimize $\mathcal{F}$ we vary $\vec{B} \rightarrow \vec{B} + \delta\vec{B}$. The first order variation in $\mathcal{F}$ is:

$$\delta\mathcal{F} = \frac{1}{\mu_0} \int d\vec{r} [\vec{B} \cdot \delta\vec{B} + \lambda_L^2 \vec{\nabla} \times \vec{B} \cdot \vec{\nabla} \times \delta\vec{B}]. \tag{3.7}$$

Using integration by parts we can replace the term $\vec{\nabla} \times \vec{B} \cdot \vec{\nabla} \times \delta\vec{B}$ by $-\vec{\nabla} \times \vec{\nabla} \times \vec{B} \cdot \delta\vec{B} = \nabla^2 \vec{B} \cdot \delta\vec{B}$ to obtain:

$$\delta\mathcal{F} = \frac{1}{\mu_0} \int d\vec{r} \left[\vec{B} + \nabla^2 \vec{B}\right] \delta\vec{B}. \tag{3.8}$$

Taking $\delta\mathcal{F} = 0$ gives the London equation:

$$\vec{B} + \lambda_L^2 \nabla^2 \vec{B} = 0. \tag{3.9}$$

In the above calculation we have shown that the existence of steady currents without driving electric fields leads to the London equation. The London equation describes perfect diamagnetism as will be shown in a simple example in the next section.

3.2 London Penetration Depth

The London equation shows that the magnetic field in the sample decays exponentially into the sample with decay constant λ_L. The detailed form of $\vec{B}$ depends on the geometry of the sample and the applied field. Let us consider a simple example: an infinite superconductor is placed in the $z > 0$ half space, so that its surface is the x-y plane at $z = 0$. The magnetic field is applied in the $\hat{x}$ direction. The magnetic field is uniform on the superconductor's surface and varies only in the $\hat{z}$ direction. In this case the London equation reduces to:

$$B_x(z) + \lambda_L^2 \frac{d^2 B_x(z)}{dz^2} = 0. \tag{3.10}$$

The solution is an exponential decay: $B_x(z) = B_x(0)e^{-z/\lambda_L}$. Note that the above calculation assumes the bulk superconductivity is not destroyed by the magnetic field and therefore the theory is valid for weak fields. This simple example can easily be generalized to other sample shapes since λ is often small compared to the macroscopic sample dimensions.

Except for the Meissner effect itself, another important prediction is the value of λ_L. We have previously shown that $\lambda_L = [\frac{m^*}{\mu_0 n_s e^2}]^{1/2}$; in other words λ_L gives the ratio of number of carriers per unit volume to their effective mass: $n_s e^2/m^*$, also called the oscillator strength since it is the pre factor of the delta function of σ_1 in zero frequency. In the limit of low temperatures we expect all charge carriers to be part of the superconducting condensate. In the context of the BSC theory [1] the carriers are pairs of electrons (known as Cooper pairs) and therefore we would expect $n_s = \frac{1}{2}n_e$, the pair's effective mass should be close to $2m_e$ and their charge is $2e$. In metals like aluminum one would find $\lambda \simeq 500\mathring{A}$. In the high T_c cuprates the carriers are believed to be holes and their concentration depends on oxygen content. In an optimally doped single crystal YBCO λ was measured to be between $800\mathring{A}$ and $2000\mathring{A}$ by μSR [8, 9] and far infrared [10].

3.3 Magnetic Penetration Depth

It is important to mention that the above calculation is only valid in the local limit, also referred to as the London limit. An assumption has been made here that both the magnetic field $\vec{B}(\vec{r})$ and the current $\vec{J}_s(\vec{r})$ vary slowly in space. In order to define what is meant by "slowly" another parameter, ξ, the coherence length, has to be introduced.

So far we have considered a supercurrent that is carried by a condensate without introducing any mechanism for the superconductivity. However, the mechanism is important for determining the relevant length scales in the problem. In 1957 J. Bardeen, L. N. Cooper and J.R. Schriffer laid the fundamentals of the theory of superconductivity known as the BCS theory [1]. The details of the theory will not be given here and can be found in reference [14]. The theory describes superconductivity as the result of pairing between electrons with equal and opposite momentum, the Cooper pairs. The ground state of the system (also called the condensate) is separated from the excited states (quasiparticles) by the energy gap, Δ. The Hamiltonian of the system contains the pairing potential and the energy of the quasiparticles (above the condensate) is given by:

$$E_k = \sqrt{\epsilon^2(k) + |\Delta(k)|^2} \tag{3.11}$$

where $\epsilon(k) = \frac{(\hbar k)^2}{2m} - \epsilon_F$ is the energy of a free electron with respect to the Fermi energy and $\Delta(k)$ is the energy gap. At low temperatures the system contains a condensate of paired electrons which exhibit frictionless motion. Excitation of quasiparticles involves pair breaking and therefore requires energy that is larger than the energy gap. This reduces substantially the probability of collisions since at low temperatures such energetic particles are not available. The gap Δ may vary in space and the coherence length, ξ, is defined as the length scale in which the gap can vary. An estimation of the coherence length can be made in the following way. The relevant kinetic energy range of our system is of the order 2Δ around the Fermi surface:

$$E_F - \Delta_0 < \frac{(\hbar k)^2}{2m} < E_F + \Delta_0 \tag{3.12}$$

where Δ_0 is the maximal gap in case of non uniform gap function. In this range of energies we can approximate $k \approx k_F + \delta k$ and $E \approx E_F + v_F \hbar \delta k$ and therefore the relevant momentum range is $\delta k \cong \frac{2\Delta}{\hbar v_F}$. This momentum span corresponds to a

spatial span of $\delta x \sim \frac{1}{\delta k}$ and the coherence length is approximately:

$$\xi = \frac{\hbar v_F}{\pi \Delta_0}. \tag{3.13}$$

The London limit holds when $\lambda >> \xi$. In this limit the correlation between electrons has a short length scale and their response to electromagnetic fields is local. In high T_c superconductors such as YBCO, ξ is of the order of several lattice constants and λ is a few thousand $\mathring{A}$ so that the London limit is valid. In other cases (elemental metals for examples) ξ may be considerably larger. In this case the free energy calculation should be modified to introduce a non-linear relation between $\vec{J}$ and $\vec{A}$.

4: Electron Spin Resonance

Our measurements of λ are obtained by applying an rf field to magnetically doped YBCO and observing Electron Spin Resonance (ESR) transitions in a dilute array of magnetic moments. This chapter will describe briefly the basic theory of magnetic resonance in general and electron spin resonance in particular.

4.1 Magnetic Resonance

Any physical system with quantized magnetic moments can exhibit magnetic resonance. Our interest is in the spin magnetic moment of the electrons in the ion. However, the following description of the magnetic resonance effect is general, where the magnetic moment $g\mu_B\vec{S}$ can be replaced by $g\mu_B\vec{J}$ where $\vec{J}$ is the total angular momentum in the system, $\vec{J}=\vec{L}+\vec{S}+\vec{I}$ where $\vec{L}$ is the angular momentum, $\vec{S}$ is the electron spin and $\vec{I}$ is the nuclei spin.

Consider a system of free spins with magnetic moment $\mu_B g\vec{S}$. Without any external magnetic field all energy levels are degenerate. Applying a uniform magnetic field in the $\hat{z}$ direction lifts the degeneracy completely. The system's new eigenstates correspond to the Zeeman levels with energy $-\mu_B g m\vec{H}$ where $m=-S\ldots S$ is the projection of the spin on the $\hat{z}$ axis. The new eigenstates of the system, labeled $|m\rangle$ are the eigenstates of $\hat{S}_z$, where $\hat{S}_z|m\rangle = m|m\rangle$. Any magnetic interaction, such as the crystal field, may lift the degeneracy in some way that would change the eigenstates of the system (for example, the crystal field lift the degeneracy of different spin orientations but does not split the Kramers doublets). In general, the new eigenstates can be described as linear combinations of the $|m\rangle$ states.

$$|\psi_n\rangle = \sum_{m=-S}^{S} a_m|m\rangle \tag{4.1}$$

For simplicity we will assume that the energy levels $|\psi_n\rangle$ are very close to the $|m\rangle$ states, and will use the $|m\rangle$ states instead. This assumption is valid for the Gd ions in YBCO but is not at all necessary for the following discussion and the generalization is straightforward. In any case, the system has quantized energy levels with lower degeneracy than without any external field. At zero temperature only the lowest en-

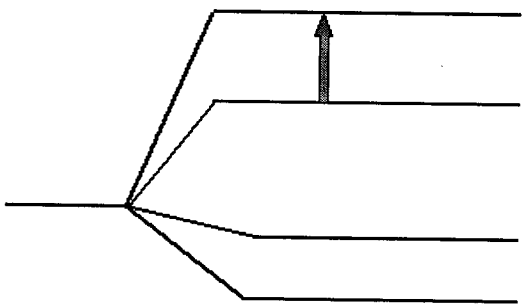

Figure 4.1: ESR transitions in a spin system. The degeneracy between the different spin orientation was lifted due to an applied magnetic field

ergy states are populated and at finite temperature each state is populated according to the Boltzmann distribution:

$$N_j = \frac{1}{z} e^{-E_j/k_B T} \quad z = \sum_i e^{-E_j/k_B T} \tag{4.2}$$

where N_j is the probability of finding an ion in the jth state with energy E_j and z is the canonical partition function. Magnetic Resonance occurs when the system absorbs or emits an energy quantum (a photon) that is equal to the spacing between two energy levels, provided the transition is allowed by quantum mechanics. A photon can be fed into the system by an alternating magnetic field of the form $\vec{H}_{rf} = \vec{H}_0 \cos(\omega t)$. This field is described by an additional perturbative term in the Hamiltonian:

$$\mathcal{H} = \mathcal{H}_0 + \mu_B g \vec{S} \cdot \vec{H}_{rf} \tag{4.3}$$

where $\mathcal{H}_0$ describes the Hamiltonian of the system without applying external AC fields and $\mu_B g \vec{S}$ is the magnetic moment). When the field is perpendicular to the principal spin axis, this term can be written as a linear combination of spin ladder operators. For example when H is applied in the $\hat{x}$ direction and the principal spin axis is $\hat{z}$ we can write:

$$\vec{S} \cdot \vec{H}_{rf} = H_{x0} \frac{1}{2} Re(S_+ e^{i\omega t} + S_- e^{-i\omega t}) \tag{4.4}$$

where $S_\pm = S_x \pm i S_y$. The new eigenstates of the system can be found from time dependent perturbation theory and can be written as a linear combination of the

eigenstates of $\mathcal{H}_0$ with time dependent coefficients:

$$|\phi(t)\rangle = \sum_m a_m(t) e^{-i\frac{E_m}{\hbar}t} |m\rangle \tag{4.5}$$

where E_m are the eigen energies of the unperturbed Hamiltonian, $\mathcal{H}_0|m\rangle = E_m|m\rangle$. Perturbation theory shows that each state $|\phi\rangle$ would oscillate between two or more $|m\rangle$ states. The transition rate (number of transitions per second) is given by Fermi's golden rule:

$$W_{ij} = \frac{\pi H_{x0}^2}{2\hbar^2} |\mu_{ij}|^2 f(\omega) \tag{4.6}$$

where $f(\omega)$ is a shape function normalized to unity and concentrated around $\omega = \frac{1}{\hbar}(E_i - E_j)$. The shape function is a result of spin relaxation processes (spin-spin interactions and/or spin-lattice interactions) and is usually a Lorentzian. μ_{ij} is defined as $\mu_{ij} = g\mu_B \langle m_j | S_{x,y} | m_i \rangle$ (x or y depend on the direction of the applied rf field) and provides the selection rules for allowed transitions.

4.2 Magnetic Ions in a Crystal: Fine Structure

A magnetic ion in a crystal experiences magnetic interactions via two mechanisms: the motion of charged particles around it (mainly electrons) and the magnetic moments (associated with the spin degree of freedom) of electrons and nuclei in the crystal. The first interaction is the fine structure of the crystal and the second one is the hyperfine interaction. Our subject of interest is a magnetic ion substitution in an otherwise non-magnetic crystal, therefore we will only consider the fine structure. A general Hamiltonian for describing this magnetic system is:

$$\mathcal{H} = \sum_{k=1}^{n} \{ \frac{1}{2m} P_k^2 - \frac{Ze^2}{r_k} + \xi(r_k) \vec{L}_k \cdot \vec{S}_k + V(r_k) \} + \sum_{k<j}^{n} \frac{e^2}{r_{jk}} \tag{4.7}$$

where n is the number of electrons associated with the ion, P_k is the kth electron's momentum, ξ_k describes the strength of the spin-orbit coupling of the kth electron and $V(r_k)$ is the potential energy of the kth electron in the electrostatic field of the environment. The second sum is the Coulomb interaction between electrons. Notice that in this picture the electrons are divided into two groups. The first contains the electrons that belong to the ion, which will be treated quantum mechanically, and the second contains environment electrons, that are expressed in $V(r_k)$ and are treated classically. Further justification and details of this picture can be found in Griffith

1961 [15].

4.3 Effective Spin Hamiltonian

The above description is a good approximation for the magnetic ion in the crystal but the form of the potential $V(r_k)$ is unknown and may have a very complicated spatial dependence. The symmetry of this Hamiltonian is very useful for further analysis. $V(r_k)$ and hence $\mathcal{H}_0$ commutes with all the elements of the point group of the ion's site in the crystal.

The effective spin Hamiltonian expresses the energy levels of the system in terms of spin operators. It is equivalent to the full Hamiltonian of the system within the subspace of a given electronic shell (constant radial wave function $R_n(r)$ and total angular momentum). It has the compact form:

$$\mathcal{H}_0 = \sum_{p,q} B_q^p O_q^p \tag{4.8}$$

where O_q^p is a Stevens operator of order q. The Stevens operators are functions of S^2, S_z, S_+ and S_- and are the operator equivalents of the spherical harmonic functions. The B_q^p are numeric coefficients that are called crystal field (CF) parameters. This sum is an expansion of the crystal field in the ion's environment in terms of a complete set of functions. We shall see that the number of elements in the sum is finite and depends on the symmetry of the crystal and the magnetic moment of the ion.

The first step in building an effective Hamiltonian is to prove that the system can be described by a finite number of parameters. One can then choose an appropriate method for calculating them theoretically, but typically the CF parameters are measured through ESR experiments. The theoretical effective spin Hamiltonian with measured CF parameters can predict the magnetic field and frequency dependence of the ESR transitions as well as their intensities and show very good agreement to the experiments.

The full proof for the CF theory is given in [15] and will not be repeated here. The basic scheme is to describe the different ionic states as Slater determinants of one-electron states and impose the site symmetry on the Hamiltonian matrix elements. The CF Hamiltonian can then be expanded in terms of spherical harmonics. Its matrix elements between ionic states are then written in terms of matrix elements of spherical harmonics between the one-electron functions, that are also described

by spherical harmonic functions. Group theory arguments show that the number of non-zero matrix elements is limited by

$$n = \frac{1}{2}\sum_j n_j(n_j + 1) - 1 \tag{4.9}$$

where j is summed over all irreducible representations of the site point group and n_j is the number of times this representation occurs in the relevant representation (according to the magnetic moment). The number n is also the number of free parameters in our problem and therefore the number of CF parameters in the effective spin Hamiltonian.

4.3.1 Semi-Classical Approach for Deriving the Effective Spin Hamiltonian

Let us assume that the crystal environment of the magnetic crystal is represented by a static charge distribution ρ. The potential energy $V(\vec{r})$ is given by:

$$V(\vec{r}) = -\int \frac{e\rho(\vec{R})}{|\vec{R} - \vec{r}|} d\vec{R}, \tag{4.10}$$

where $\vec{r}$ is the position of the electron and $\vec{R}$ is a general point in the environment. We define the environment as the space outside the magnetic ion and therefore if both $\vec{r}$ and $\vec{R}$ are measured from the nuclei then $|\vec{r}| < |\vec{R}|$. We can expand the potential in Legendre polynomials:

$$\frac{1}{|\vec{R} - \vec{r}|} = \sum_{k=0}^{\infty} \frac{r^k}{R^{k+1}} P_k(cos(\Omega)) \tag{4.11}$$

where Ω is the angle between $\vec{R}$ and $\vec{r}$. We proceed by expanding each P_k further in terms of spherical harmonics. It is convenient however to use a different basis set, Z_{lm}, instead of the regular spherical harmonics Y_{lm}:

$$\begin{cases} Z_{l0} = Y_{l0}, \\ Z^c_{lm} = \frac{1}{2}\sqrt{2(Y_{l-m} + Y_{lm})}, \\ Z^s_{lm} = \frac{i}{2}\sqrt{2(Y_{l-m} - Y_{lm})} \end{cases} \tag{4.12}$$

The above functions are all real, with Z^c and Z^s being functions of $\cos(m\phi)$ and $\sin(m\phi)$ respectively. The vector space spanned is the same as for the usual spherical

harmonics. The expansion of the Legendre polynomials in terms of Z_{lm} is:

$$P_k(cos(\Omega)) = \frac{4\pi}{2k+1} \sum_{\alpha} Z_{k\alpha}(1) Z_{k\alpha}(2) \tag{4.13}$$

where (1) refers to the coordinates (θ, ϕ) of the general point $\vec{R}$ and (2) refers to (θ, ϕ) of the electron position $\vec{r}$. The sum over α is over all the Z_{lm} functions of the same l including Z_{l0} and $Z_{lm}^{c/s}$ for $m \neq 0$. Inserting this expansion into our expression for $V(\vec{r})$ (by performing the integration over $\vec{R}$) we obtain the potential V in terms of the electron coordinates, (r, θ, ϕ):

$$V(r, \theta, \phi) = \sum_{k=0}^{\infty} \sum_{\alpha} r^k \gamma_{k\alpha} Z_{k\alpha}(\theta, \phi) \tag{4.14}$$

where $\gamma_{k\alpha}$ are characteristic numbers of the environment and are defined by:

$$\gamma_{k\alpha} = -\frac{4\pi e}{2k+1} \int \frac{\rho(\vec{R}) Z_{k\alpha}(\theta, \phi)}{R^{k+1}} d\vec{R}. \tag{4.15}$$

Since the ionic wave functions are Slater determinants of one-electron wave functions (the spherical harmonics $|l, m\rangle$ times a radial function) all matrix elements of $V(\vec{r})$ are of the form: $M = \langle l, m | Z_{k\alpha} | l, m \rangle$ times the average radius $\langle \bar{r} \rangle$. The average radius is only a numerical constant since the effective Hamiltonian is defined within the subspace of the same radial dependence. Different l functions are not included since we consider only electrons outside of the core, within one unfilled shell. The ϕ dependence of the spherical harmonics shows that the matrix element M is non-zero only when $k \leq 2l$. The parity operator is a member any site symmetry group and represents time reversal symmetry. This imposes an additional condition, that k must be even. This reduction of the number of CF parameters can be applied to every crystal. More symmetry in the system reduces the number of CF parameters even further. Any $Z_{k\alpha}$ function that violates the one or more symmetries of the system do not appear in the expansion. The above matrix elements depend only on the angular momentum degrees of freedom and can be described as equivalent operators (the Stevens operators) whose derivation can be found in [16]. A full list of the Stevens operators up to the sixth order can be found in [17].

It is important to mention that even if the semi-classical picture that is given here is not accurate, the expansion of $V(\vec{r})$ in Stevens operators is still justified since it is an expansion in an orthonormal basis that spans the chosen subspace. The cancelation

of many terms due to symmetry and orthogonality remains valid since the symmetry of the site can be imposed on the elements in the sum. However, the coefficient of each operator in the expansion may very well be different from what is calculated in this simple picture. The CF parameters can be corrected in several theoretical ways [18] and through experimental measurements (such as the work described here).

4.4 Zero field ESR and the ESR Spectrum

This section will discus the principle of ESR experiments in general with emphasis on zero field ESR. Most ESR experiments are performed with H_{rf} at a constant frequency so that ESR transitions can only occur at the relevant energy $\hbar\omega$. In other words, the perturbation to the Hamiltonian is proportional to $Re(S_+e^{i\omega t} + S_-e^{-i\omega t})$, where ω is constant. At this frequency transitions will occur only if

$$\Delta E = E_j - E_i = \hbar\omega. \tag{4.16}$$

To observe the various transitions between different pairs of states the energy levels must be shifted so that the difference ΔE matches the applied frequency. This is done by applying a DC magnetic field, usually parallel to the principal axis of the ion's spin. In this way each energy level E_m, that corresponds to a state $|m\rangle$ (an eigenstate of the S_z operator or a mixture of states that is dominated by $|m\rangle$) will gain an additional energy of $-\mu_B g m H$. This field would also lift the degeneracy associated with time reversal symmetry (the Kramers doublets of$|\pm m\rangle$). The full Hamiltonian is then:

$$\mathcal{H} = \mathcal{H}_0 + g\mu_B H_{x0}\frac{1}{2}Re(S_+e^{i\omega t} + S_-e^{-i\omega t}) + g\mu_B H'_z S_z. \tag{4.17}$$

The magnitude of the field H'_z can be changed so that each transition will occur at the frequency ω but at different H'_z field as shown in figure 4.2 for a spin $\frac{3}{2}$ system.

Another way to observe the transitions is to take the zero field ESR approach. In this situation the experiment is performed without any applied parallel field H'_z. In order to see all the possible transitions, it is necessary to scan a wide range of frequencies. The observable quantity is the absorbed power in the ESR transitions or the imaginary part of the magnetic susceptibility, χ''. These quantities can be inferred from the energy change rate (from Fermi's golden rule).

$$\frac{dE_{ij}}{dt} = W_{ij}(N_i - N_j)\hbar\omega = \frac{\pi H_{x0}^2}{2\hbar^2}|\mu_{ij}|^2 f(\omega)N_i(1 - e^{-\frac{\hbar\omega}{k_B T}})\hbar\omega \tag{4.18}$$

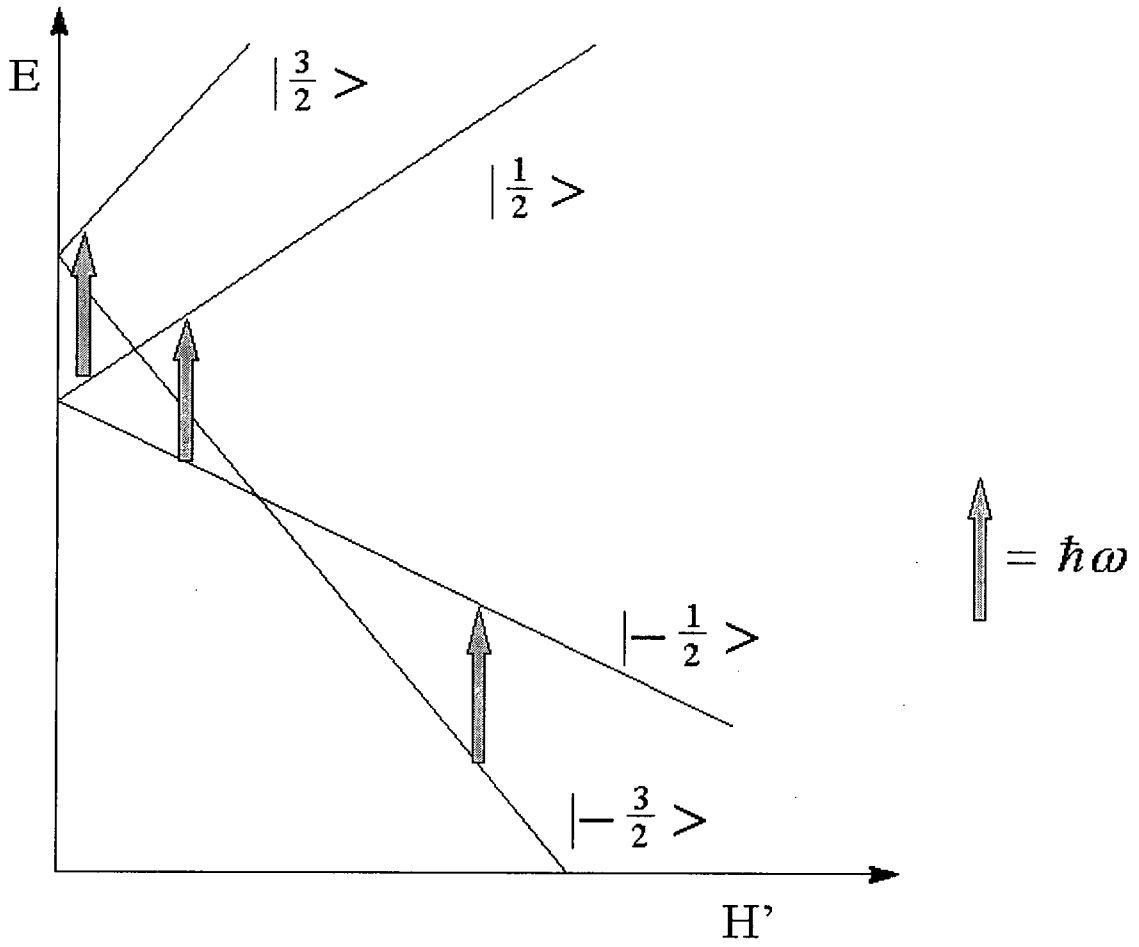

Figure 4.2: ESR transitions at a constant frequency and varying DC magnetic field for a spin $\frac{3}{2}$ system. The splitting in $H'_z = 0$ is the fine structure (where $|\pm\rangle$ states are degenerate. When H'_z is varied, the levels evolve according to their magnetic moment $g\mu_B m$.

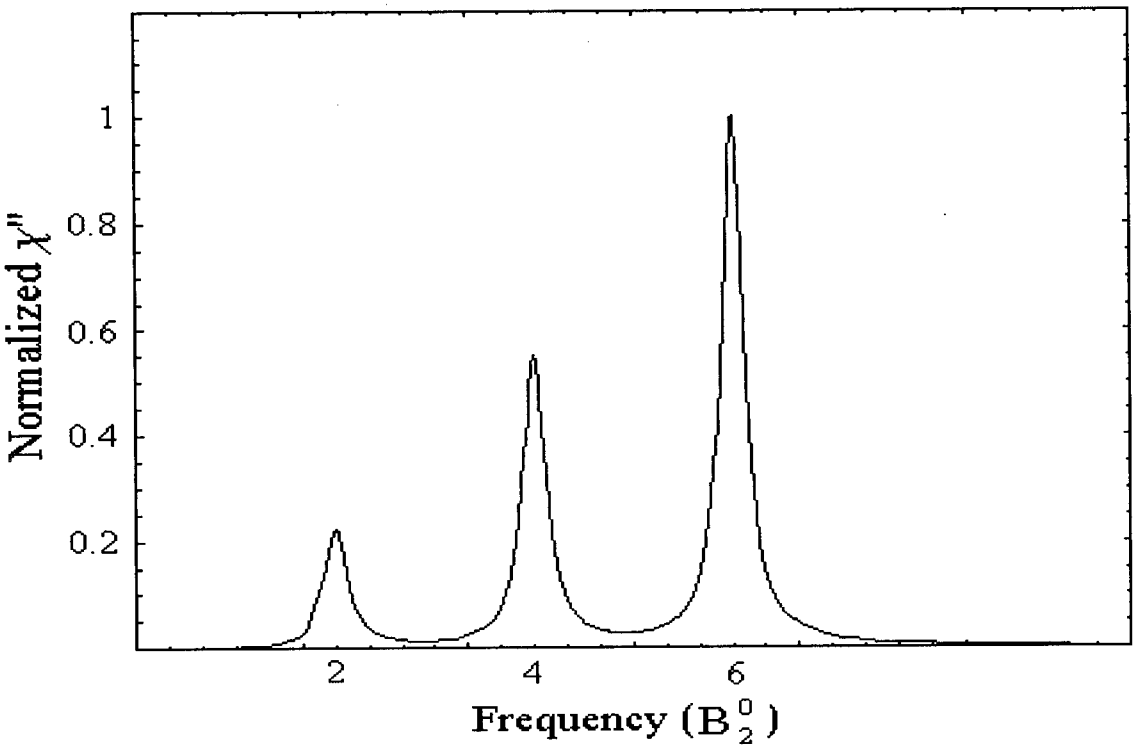

Figure 4.3: Theoretical $\chi''(\omega)$ for a system with spin $\frac{7}{2}$ and fine structure Hamiltonian $\mathcal{H}_0 = B_2^0 O_2^0 = B_2^0(3S_z^2 - S^2)$. The allowed transitions, $\pm\frac{1}{2} \rightarrow \pm\frac{3}{2}$, $\pm\frac{3}{2} \rightarrow \pm\frac{5}{2}$ and $\pm\frac{5}{2} \rightarrow \pm\frac{7}{2}$, occur at $2B_2^0$, $4B_2^0$ and $6B_2^0$ respectively. A Lorentzian shape function of width $0.06B_2^0$ has been assumed

where W_{ij} was defined in equation 4.6. From the relation $\frac{dE_{ij}}{dt} = \frac{1}{2}H_{x0}^2\omega\chi''$ we get the susceptibility:

$$\chi''_{ij}(\omega) = \frac{\pi}{\hbar}|\mu_{ij}|^2 f(\omega)N_i(1 - e^{-\frac{\hbar\omega}{k_B T}}) \tag{4.19}$$

where the average number of spins in the ith level, N_i, is given by the Maxwell-Boltzmann distribution:

$$N_i = N\frac{1}{z}e^{-E_i/k_B T} \tag{4.20}$$

where N is the total number of spins per unit volume and $z = \sum_j e^{-E_j/k_B T}$is the partition function. The total χ'' is a sum of shape functions, centered around the frequencies of allowed ESR transitions with an integrated intensities of $\frac{\pi}{\hbar}|\mu_{ij}|^2 N_i(1 - e^{-\frac{\hbar\omega}{k_B T}})$. Figure 4.3 shows a typical susceptibility spectrum for a Hamiltonian $\mathcal{H}_0 = B_2^0 O_2^0 = 3S_z^2 - S^2$ and spin $\frac{7}{2}$. In a $\frac{7}{2}$ spin system the energy levels are $E_m = B_2^0(m^2 - \frac{7}{2}\cdot\frac{9}{2})$ and the ESR transitions appear at $\hbar\omega = E_{m+1} - E_m = B_2^0(2m+1)$ i.e at $2B_2^0$, $4B_2^0$ and $6B_2^0$.

5: The Bolometric Experiment

Performing zero field ESR on magnetic ions embedded in a superconducting sample involves measuring $\chi''(\omega)$ at a low temperature over a wide range of frequencies. In the next chapter it will be shown that the susceptibility and the surface resistance are related through:

$$\chi''(\omega) = \frac{Rs^{ESR}}{\frac{1}{2}\mu_0\omega\lambda_L} \tag{5.1}$$

where R_s^{ESR} is the contribution of the magnetic impurities to the sample's surface resistance and λ_L is the London penetration depth. This relation was used to extract the susceptibility from surface resistance measurements. The experimental part of this project was performed by Patrick J. Turner in an existing bolometric apparatus [19] which has been developed in the UBC superconductivity lab as a sensitive probe of the microwave surface resistance of high T_c samples. Measurements can be carried out over a range of temperatures (1.3-10K)and over a broad band of microwave frequencies (0.1-21GHz).

The choice of performing zero field ESR through a broadband measurement of surface resistance was made for several reasons. The first, practical, reason was the existing surface impedance measurement facilities in our lab. An early idea was to measure the real part of the susceptibility, $\chi'(T)$, through surface reactance measurement at very low frequency (10kHz) where the imaginary part, χ'', is negligible. This would be essentially a measurement of the DC susceptibility of the spins that are exposed to the magnetic field and therefore the magnitude should be proportional to the penetration depth. The effect of magnetic impurities on $R_s(T)$ is an upturn at low temperatures since $X_s \propto \sqrt{1+\chi'}$. This upturn is a result of the $1/T$ paramagnetic temperature dependence of $\chi'(T)$. However, the first order contribution to the DC response comes only from the $-\frac{1}{2} \rightarrow +\frac{1}{2}$ transition between the spin levels of the ion, while the higher spin transitions only contribute in the second order to the susceptibility. DC measurement of χ' would show the expected upturn, but the Gd contribution to this effect is actually quite small and might not be easily distinguished from other magnetic contributions (such as $BaCuO$ flux on the sample's surface). An alternative approach was therefore taken.

It was a fortunate coincidence that an apparatus existed in the lab which is capable

of measuring the frequency dependence of R_s over the range where the zero field ESR peaks exist. The AC response of the sample, $\chi''(\omega)$, involves first order spin transitions at certain frequencies (the ESR transitions). The frequency of the transitions together with their intensity provides the information needed to determine the number of ions exposed to the field (see chapter 6). The bolometric experiment was found to have both sufficient sensitivity and appropriate range of frequencies to reveal the ESR lines for this particular system. Our knowledge of the relevant frequency range was based on the crystal field parameters as measured in conventional ESR [20, 21, 22, 23, 24].

Furthermore, zero field ESR (rather than conventional ESR) is done in the same field configuration as other microwave measurements at UBC. The samples are usually very thin in the $\hat{c}$ direction compared with the dimensions of the a-b plane. The field is applied along the $\hat{a}$ ($\hat{b}$) direction with the currents running mainly in the a-b plane. In this configuration the magnetic field is hardly distorted by the sample. On the other hand, conventional ESR must be done with external magnetic field along the $\hat{c}$ direction. In this configuration the field is distorted by the relatively large area of the a-b plane and the resulting demagnetization effects are much larger.

An additional advantage of the chosen method is the ability to isolate the ESR lines from other features in our data. The susceptibility $\chi''(\omega)$ is extracted from the measured surface resistance as explained in section 6.3. The first step in this extraction is to separate the Gd contribution to the surface resistance, $R_s^{ESR}(\omega)$, from the superconductor surface resistance, $R_s^{SC}(\omega)$. For YBCO, $R_s^{SC}(\omega)$ is known to be a smooth monotonic function of frequency, that can be fitted by a low order polynomial function. An example for this functional form is shown in figure 5.2. On the other hand, R_s^{ESR} is a sum of sharp Lorentzians with widths of about 250MHz. The total surface resistance, as measured by the bolometric experiment is the sum of the two, but the two components can be easily separated thanks to their different shape.

5.1 The Measurement Principle

Microwave measurement of the surface resistance of YBCO samples have been performed in the UBC superconductivity lab since 1989. The typical measurement technique is cavity perturbation (this method is described in A). A resonator is designed to have a resonance frequency with high quality factor (Q). The sample's surface impedance, Z_s, is measured at this particular frequency over a wide range of temperatures. Different resonators in different frequencies were designed, and R_s of various

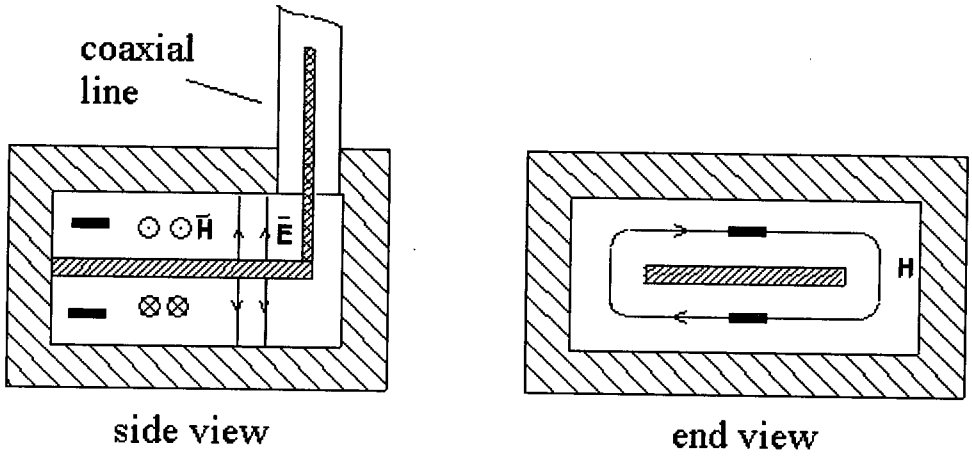

Figure 5.1: The electromagnetic fields configuration in the bolometric apparatus. The sample and reference are the black rectangles

YBCO samples were obtained [7, 4]. The bolometric technique was developed to complete the resonator data over a broad band of microwave frequencies in order to show the detailed frequency dependence of the surface resistance.

The basic idea behind the bolometric technique is to measure the sample's surface resistance through its power absorption in a microwave magnetic field. This is done using a reference sample (in our case a high purity Ag:Au alloy) of known surface resistance. The sample and the reference are inserted into a shorted transmission line in two positions that have nominally the same magnetic field configuration. The thermal response of the reference and the sample due to their rf absorption are measured as a function of microwave frequency. As shown in appendix C, since the two samples experience the same tangential magnetic field on their surface, it follows that the ratio of power absorption is also the ratio between their surface resistances:

$$\frac{P^{sample}}{P^{reference}} = \frac{R_s^{sample}}{R_s^{reference}}. \tag{5.2}$$

Using the power ratio, the sample's R_s is inferred from the known R_s of the reference.

Implementing this measurement requires a setup with a microwave magnetic field that is uniform over the dimensions of both samples, is equal in the positions of the sample and the reference, and whose frequency can be varied continuously . The experiment is designed as a rectangular termination of a coaxial transmission line. The field configuration near the end of the line is shown in figure 5.1. At the termination, the center conductor is a broad flat rectangle. This provides a symmetric

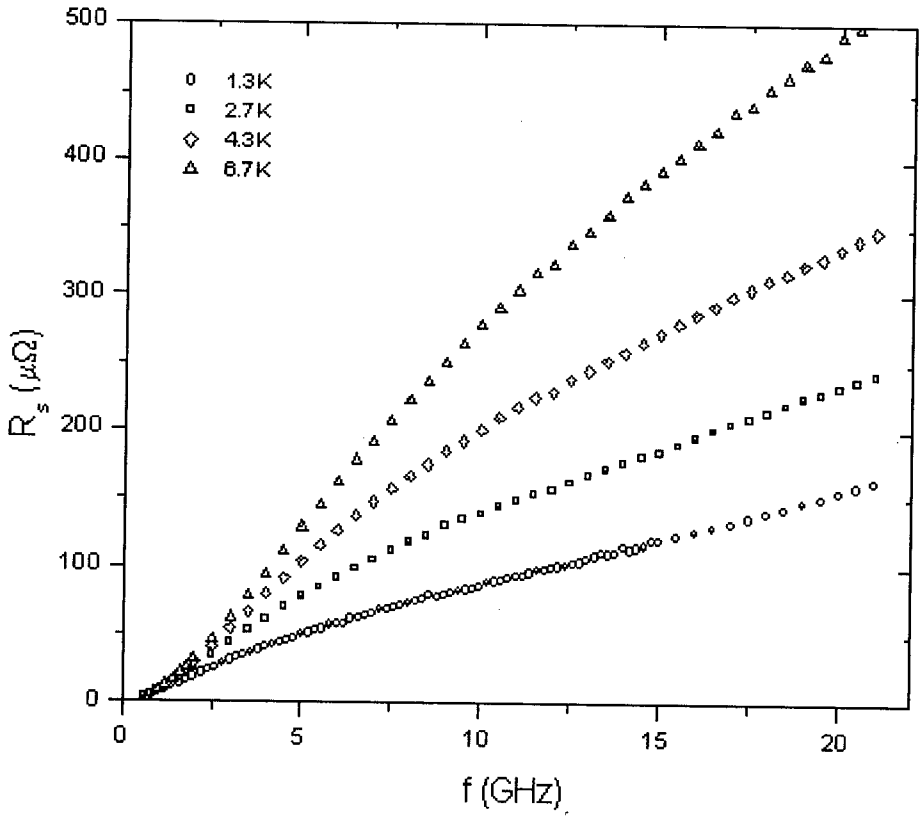

Figure 5.2: A typical surface resistance spectrum of a YBCO sample at different temperatures as measured in the bolometric apparatus

magnetic field that is reasonably uniform in the regions of the sample and reference. This design supports a non-resonant TEM mode with a magnetic antinode and an electric node near the sample and the reference.

The sample holder is designed as a cold finger, a technique that was first described by Sridhar and Kennedy [25]. This technique provides an isothermal connection (sapphire plate) between the sample and the thermometer and a weak link to a pumped helium bath. This permits temperature oscillations of the sample, while ensuring that the time constant for the stage to cool, following power input, is not too long [19].

6: λ Extraction Technique

Having introduced the bolometric measurement technique and the concept of ESR we are now ready to combine these two types of experiments into a new direct method of measuring the London penetration depth of superconductors. The main idea here is to dope the superconductor with magnetic ions that serve as magnetic indicators. Ions that reside close to the sample's surface, within the penetration depth, are exposed to the magnetic field. Only these ions participate in the ESR process and therefore contribute to the line intensity of the various transitions. Ions deep inside the superconductor experience no magnetic field and therefore will not participate in the ESR process. The resulting frequency-integrated intensity of each ESR transition is proportional to the effective number of spins that are exposed to the field which can then be related to the penetration depth λ. The following sections describe how this principle was applied to YBCO with Gd impurities.

6.1 The Samples

The material of interest is $YBa_2Cu_3O_{7-\delta}$. The magnetic dopant chosen for this study was gadolinium (Gd) in the yttrium site, so that the doped crystal is $Gd_xY_{1-x}Ba_2Cu_3O_{7-\delta}$. This substitution is ideal for several reasons. First, the yttrium site lies halfway between the copper-oxygen bilayer (see the unit cell of YBCO in figure 6.1). As indicated by the relatively low conductivity along the $\hat{c}$ direction [26], transport is primarily in the copper-oxygen planes. Choosing a dopant site outside of the planes reduces the effect of the substitution on the scattering mechanism in the $\hat{a}$ and $\hat{b}$ directions. We expect the extracted λ to be similar to that of an undoped superconductor.

Gadolinium is a rare-earth ion with an oxidation number of +3 (the same as yttrium) and substitutes only on the yttrium site. Another advantage of the Gd ion is its ESR spectrum. The Gd^{+3} ion has an exactly half filled f-shell: the f orbital has angular momentum $L = 3$ and therefore $2 \times (2 \times 3 + 1) = 14$ states. The shell is half filled by the seven remaining electrons (after 3 electrons have left the atom). Such a half-filled shell has total orbital angular momentum of zero. As a result, the ion's magnetic moment comes solely from the spin of the seven electrons and the system is a nearly free spin $\frac{7}{2}$ system. Thus, the total angular momentum is $S = \frac{7}{2}$ and there is only one

angular momentum multiplet, instead of the usual $J = L + S \ldots |L - S|$ multiplets. This simplifies the ESR spectrum which has only three main lines, corresponding to the transitions: $\pm\frac{1}{2} \rightarrow \pm\frac{3}{2}$, $\pm\frac{3}{2} \rightarrow \pm\frac{5}{2}$ and $\pm\frac{5}{2} \rightarrow \pm\frac{7}{2}$. Moreover, the splitting of the levels (resulting from the fine structure in the Y/Gd site) are of order 1-15 GHz so that all of the transitions fall within the frequency range of our bolometric apparatus. Our present study has benefitted considerably from previous work on Gd doped YBCO by A. Janossy *et al.* [21, 22, 23], S.Pekker *et al.* [27] and A. Rockenbauer*et al.* [24]. Their work was conventional ESR in applied fields of aligned $Gd_xY_{1-x}Ba_2Cu_3O_{7-\delta}$ powder samples. These experiments measured the CF parameters of the Gd site for several oxygen contents in a variety of underdoped samples. In this work, we use the conventional ESR measured CF parameters as first guesses for our spin Hamiltonian.

6.1.1 Sample Preparation

The gadolinium doped samples were prepared by Dr. Ruixing Liang of the UBC Superconductivity Lab. The procedure is very similar to the one used for making high purity YBCO crystals [28, 29].

Growth of YBCO crystals typically begins with powders of Y_2O_3, $BaCO_3$, and CuO. In the case of gadolinium substitution, a gadolinium-oxide powder is added (Gd_2O_3). The ratio of gadolinium-oxide to yttrium-oxide sets the nominal Gd concentration. However, the precise concentration in the crystal has to be determined by other means.

The rest of the process is identical to YBCO single crystal preparation. A ceramic crucible ($BaZrO_3$) filled with a mixture of the above powders is placed in a furnace and then heated up to 1000^oC for 12-24 hours until the powders melt completely. The heating is done near the edge of the furnace and next to a quartz rod that serves as a cold finger to create a horizontal temperature gradient towards the center of the furnace. The temperature gradient, of $2 - 5^oC/cm$, improves the growth stability and enhances the growth rate. Once a uniform melt is obtained, the temperature is lowered slowly and at about 985^oC crystals start to form near the coldest spot on the crucible.

Post annealing is done slightly below growth temperature in pure oxygen flow to release residual strain and defects. A lower temperature anneal is used to set the oxygen content, which is a function of the annealing temperature and oxygen partial pressure [30].

The crystals grow naturally twinned so that the $\hat{a}$ and $\hat{b}$ directions are mixed (the

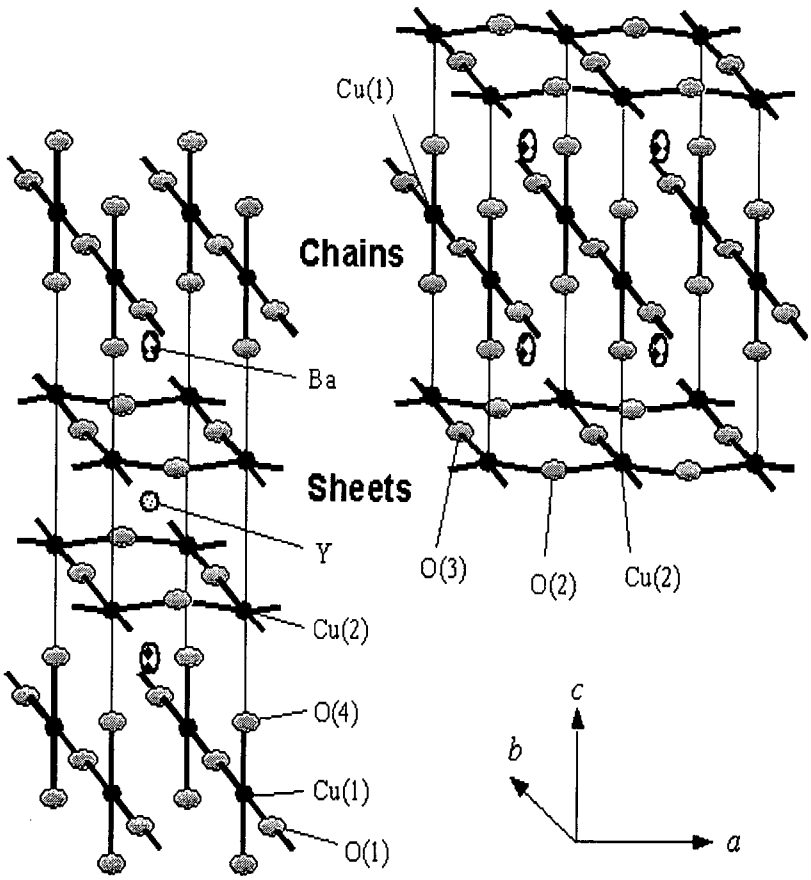

Figure 6.1: The YBCO unit cell. Gadolinium substitutes into the yttrium site. The left picture shows one unit cell and the right picture focuses on the Cu-O chains along the $\hat{b}$ axis.

so-called twins). The twins are removed by heating the sample to $200 - 400°C$ and carefully applying pressure along one direction in the a-b plane. This procedure is called detwinning.

Another important issue is the crucible material. The $BaO\text{-}CuO$ melt is highly corrosive and reacts with most materials typically used for crucibles. Extensive study has led to the currently used $BaZrO_3$ crucibles. These crucibles replaced the widely used YSZ (Y_2O_3 stabilized ZrO_2) to create the high purity new generation crystals of 99.995% atomic purity [?, ?].

6.1.2 Gadolinium Concentration Determination

The Gd concentration in the crystal is not necessarily equal to the concentration in the starting oxide powders and has been found that the actual Gd concentration can be substantially higher than in the starting powders. This difference in concentration is a result of growing the crystal from a liquid melt. The Gd ions migrate preferably into the crystal rather than the melt, and as a result the Gd concentrations in the crystal is higher than initially expected.

One way to determine the Gd concentration of the samples is by the Curie-Weiss susceptibility in the normal state using a SQUID magnetometer. The samples were measured in a field of 2T applied parallel to the $\hat{a}$ ($\hat{b}$) direction and the magnetization was measured for temperatures between 100 and 300K, above the critical temperature of the superconductor, T_c. In this field direction and temperature range, the susceptibility of YBCO is constant. The resulting magnetization is mainly due to the Gd paramagnetic contribution to the DC susceptibility and therefore obeys the Curie-Weiss law [31]:

$$\chi(T) = \frac{C}{T - T_{Weiss}} + \theta \tag{6.1}$$

where C is the Curie constant and is given by:

$$C = \frac{NS(S+1)g^2\mu_B^2}{3k_B}. \tag{6.2}$$

and θ is the constant YBCO susceptibility. The data is fitted to equation 6.1 and the constant C is determined. A ceramic powder sample of $Gd_xY_{1-x}Ba_2Cu_3O_{7-\delta}$ with known $x = 0.01$ was used as a concentration standard. The concentration of Gd in the powder is known since its growth procedure does not include separating the crystal from the melt in any stage (thus all of the input materials end up in the sample and nothing in wasted). It was found that $T_{Weiss} = -0.5 \pm 2K$ and $g = 2.03 \pm 0.01$.

6.2 R_s and χ''

In a superconducting sample with magnetic doping the observed surface resistance has two components: one comes from the lossy part of the diamagnetic shielding current that is assumed to be independent of the magnetic doping (for small doping) and is a monotonic smooth function of frequency (as shown for a typical YBCO sample in figure 5.2 in chapter 5). The other contribution comes from the transitions between the Gd spin levels (the so-called ESR transitions). The magnetic susceptibility χ'' and the ESR component of the surface resistance R_s^{ESR} are related in the following way:

$$\chi'' = \frac{R_s^{total} - R_s^{sc}}{\frac{1}{2}\mu_0\omega\lambda} = \frac{R_s^{ESR}}{\frac{1}{2}\mu_0\omega\lambda} \tag{6.3}$$

where R_s^{total} is the measured surface resistance and R_s^{sc} is the superconductor's surface resistance. This can be derived from the expression for surface impedance $Z_s = R_s + iX_s$, as is now shown. At low temperature (in the superconducting state) $R_s \ll X_s$ and we can make the following approximation:

$$Z_s^2 = R_s^2 - X_s^2 + 2iX_sR_s \approx -X_s^2 + 2iX_sR_s. \tag{6.4}$$

On the other hand we can modify equation 2.14 to include the magnetic response of the Gd ions:

$$Z_s = (\frac{i\mu\omega}{\sigma_1 - i\sigma_2})^{\frac{1}{2}} \quad with \quad \mu = \mu_0(1 + \chi' - i\chi'') \tag{6.5}$$

where the permeability μ replaces μ_0 to account for the magnetic moments in the sample. In the superconducting state $\sigma_2 \gg \sigma_1$ at any low frequency, and therefore Z_s^2 reduces to

$$Z_s^2 = \frac{\mu_0\omega}{\sigma_2^2}[-(1 + \chi')\sigma_2 + i((1 + \chi')\sigma_1 + \chi''\sigma_2)]. \tag{6.6}$$

Comparing equations 6.4 and 6.5 we obtain:

$$X_s^2 = \frac{\mu_0\omega}{\sigma_2}(1 + \chi') \quad and \quad R_s = \frac{\mu_0\omega}{\sigma_2^2}\frac{1}{2X_s}[(1 + \chi')\sigma_1 + \chi''\sigma_2]. \tag{6.7}$$

For a dilute array of paramagnetic moments we can assume $\chi' \ll 1$. In our system, a rough estimation of χ' was done in the following way. The real and imaginary parts of the susceptibility are related through Kramers-Kronig relation. Since the $\chi''(\omega)$ depend on frequency only in the shape function, $\chi'(\omega)$ for each transition would be the integrated intensity of χ'' times the Kramers-Kronig transform of the shape function. For a Lorentzian shape function with width η, the maximum of the transformed

function is $1/2\eta$. Therefore, the maximal value of χ' is:

$$\chi'(\omega)_{max} = A\frac{1}{2\eta} \tag{6.8}$$

where A is the integrated intensity of the largest ESR transition. In our system this gives $\chi' \approx 10^{-7}$ and therefore we can approximate $1+\chi' \approx 1$ in the above expressions. Finally, with $\sigma_2 = \frac{1}{\mu_0\omega\lambda^2}$ we obtain:

$$R_s = \frac{1}{2}\mu_0^2\omega^2\lambda^3(\sigma_1 + \frac{\chi''}{\mu_0\omega\lambda^2}) \tag{6.9}$$

and result 6.3 follows.

6.3 Background Subtraction

The extraction of χ'' from our measured R_s involves subtracting the superconductor's surface resistance (R_s^{sc}) from the total measured surface resistance. This is done by fitting a polynomial function to the surface resistance data between the ESR peaks (at places that are far enough from any Lorentzian tail) and subtracting this fit from the total surface resistance. This fitting procedure was found to be the best solution for separating the two contributions. The functional form of R_s^{sc} is unknown but it has been seen in various samples to be a smooth function of frequency. Another approach would have been to subtract R_s data from a different sample (YBCO without Gd doping) but so far this approach has failed since for the samples tried the background level is sample dependent, not surprising since it is very sensitive to surface quality.

The next chapter discusses the results and the data is presented in figures 7.2 and 7.5 as the measured surface resistance with a polynomial curve fitted to the background between the ESR peaks.

6.4 Spectrum Fitting and Extraction of λ

Once the background is subtracted, the ESR spectrum is ready to be analyzed. We have obtained $R_s^{ESR} = R_s^{total} - R_s^{SC}$. Dividing this data by frequency gives χ'' up to a factor of $\pi\mu_0\lambda$. In order to extract λ one must first calculate χ'' from the Hamiltonian of the system. Our strategy was to use CF parameters that were measured in conventional ESR experiments [24, 27, 21, 22, 23] as a first guess and make some adjustments to fit our own data. To do this a Mathematica notebook was written by

Richard Harris (see appendix B). The algorithm receives the crystal field parameters and returns the susceptibility function. The procedure is the following:

- Build a matrix presentation of the Hamiltonian given parameters, $\mathcal{H}_0 = \sum_{p,q} B_q^p O_q^p$, in the subspace of spin $\frac{7}{2}$.
- Diagonalize $\mathcal{H}_0$ to find the eigenvalues which are the system's energy levels.
- Calculate all matrix elements of S_x or S_y, according to the polarization of the rf field. Every matrix element that is non zero is an allowed transition and would be observed as a peak in the spectrum at $\hbar\omega = \Delta E$
- For every allowed transition, the transition energy is calculated by $E_{ij} = E_i - E_j$ and the intensity of the transition is calculated from equation 4.19 using the eigen values of $\mathcal{H}_0$.
- Build the $\chi''(\omega)$ spectrum as a sum of shape functions (Lorentzians) centered around the calculated transition energies. The width of the peaks is taken from the experiment, but the total intensity was calculated before.
- After the spectrum is calculated it can be compared with the experimental spectrum. If the calculated resonances are not exactly at the same frequencies as the experimental ones, the CF parameters are adjusted to fit the data and the procedure is repeated with the new parameters.
- The unknown parameter λ is chosen to give the best agreement between the calculated and experimental spectrum. This is done by fitting the experimental data with a sum of Lorentzians and obtaining the area of the largest transition, A, where the background subtraction error is lowest. λ is extracted by comparing this area, A, with the theoretical one: $A = \frac{1}{2}\mu_0\lambda\frac{\pi}{\hbar}|\mu_{ij}|(N_i - N_j)$ where the relevant matrix element, partition function and energies were calculated by the program discussed above.

7: Results and Analysis

Before performing any experiment, a prediction of the ESR spectrum was generated. The crystal structure has a nearly tetragonal symmetry (with about 1% difference between the $\hat{a}$ and $\hat{b}$ dimensions) and very high anisotropy in the $\hat{c}$ direction as compared to the a-b plane. Considering all the Stevens operators from O_2^0 and higher, the following reductions should apply. The system has spin $\frac{7}{2}$ with no orbital angular momentum and therefore the highest order Stevens operator that should be considered is 6 (since $k \leq 2S$ where k is the order of the operator and S is the total angular momentum, k is also even). In addition, since the a-b plane has approximately $\frac{\pi}{2}$ rotational symmetry, all of the operators that violate this symmetry (the O_k^2) should have negligible CF coefficients. The operators that survive this selection are: $O_2^0, O_4^0, O_4^4, O_6^0, O_6^4$ and O_6^6. Given the dimensions of the unit cell, we expect that the diagonal terms, O_k^0, be larger than the off-diagonal terms. Combining this with the fact that this sum is an expansion, the dominant term in the Hamiltonian is O_2^0. The expected spectrum would contain three main transitions, since the eigenstates of the system are the Kramers doublets, $| \pm m >$. The spacing between the ESR lines of a system with $\mathcal{H}_0 \propto O_2^0$ is constant since $O_2^0 = 3S_z^2 - S^2$ (as was shown in figure 4.3). However, in our system the spacing between lines may not be constant due to additional CF parameters (mainly O_4^0).

7.1 Twinned Optimally Doped Crystal

The first measurement was performed on a twinned 1.28% Gd doped $YBa_2Cu_3O_{6.92}$ crystal. The surface resistance results are shown in figure 7.1 along with a polynomial fit to the background. A spectrum proportional to χ'' was obtained by subtracting the background fit and dividing by frequency as shown in figure 7.2. Note that the spectrum contains six sharp ESR peaks. This is in contradiction to the predicted spectrum. Any reasonable combination of the above operators could not yield such a spectrum and the solution to the problem was eventually found elsewhere.

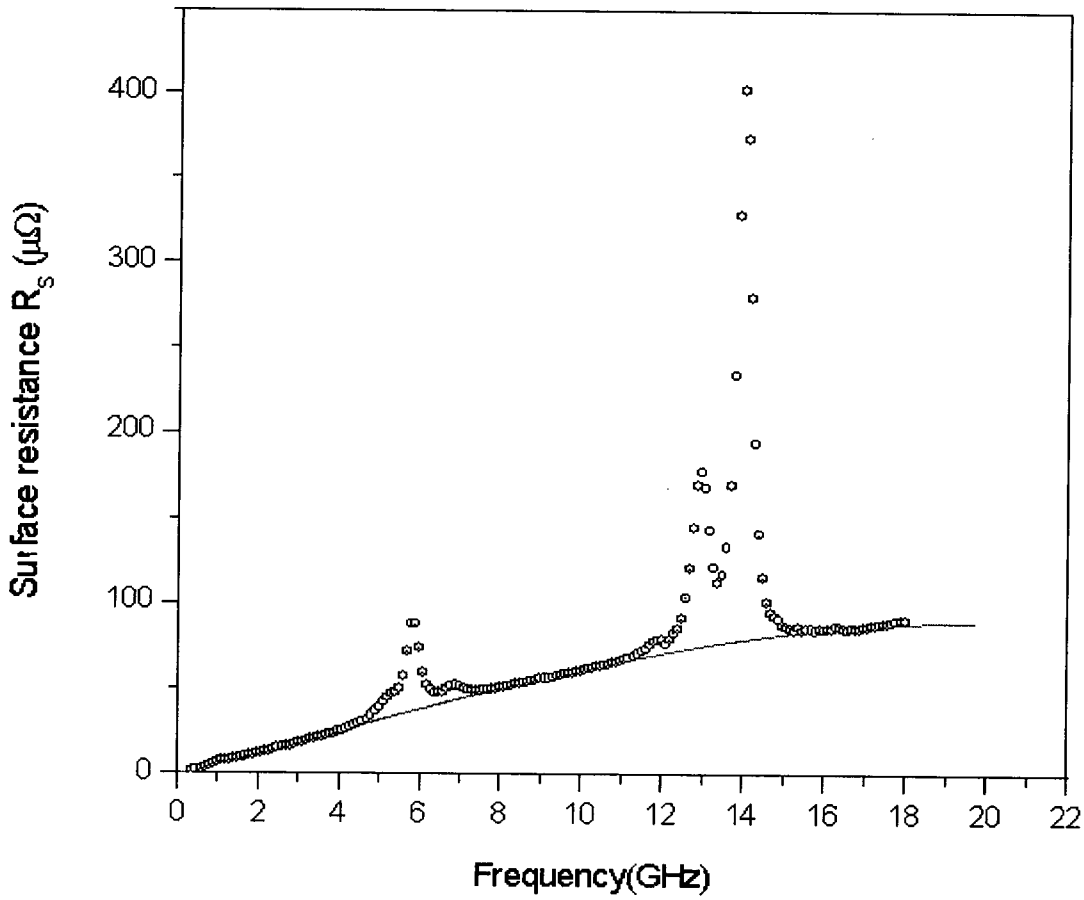

Figure 7.1: The surface resistance of a twinned optimally doped sample with 1.28% Gadolinium - $Gd_{0.01}Y_{0.99}Ba_2Cu_3O_{6.92}$. The graph shows the full surface resistance (points) with a polynomial fit to the background between the ESR peaks (line).

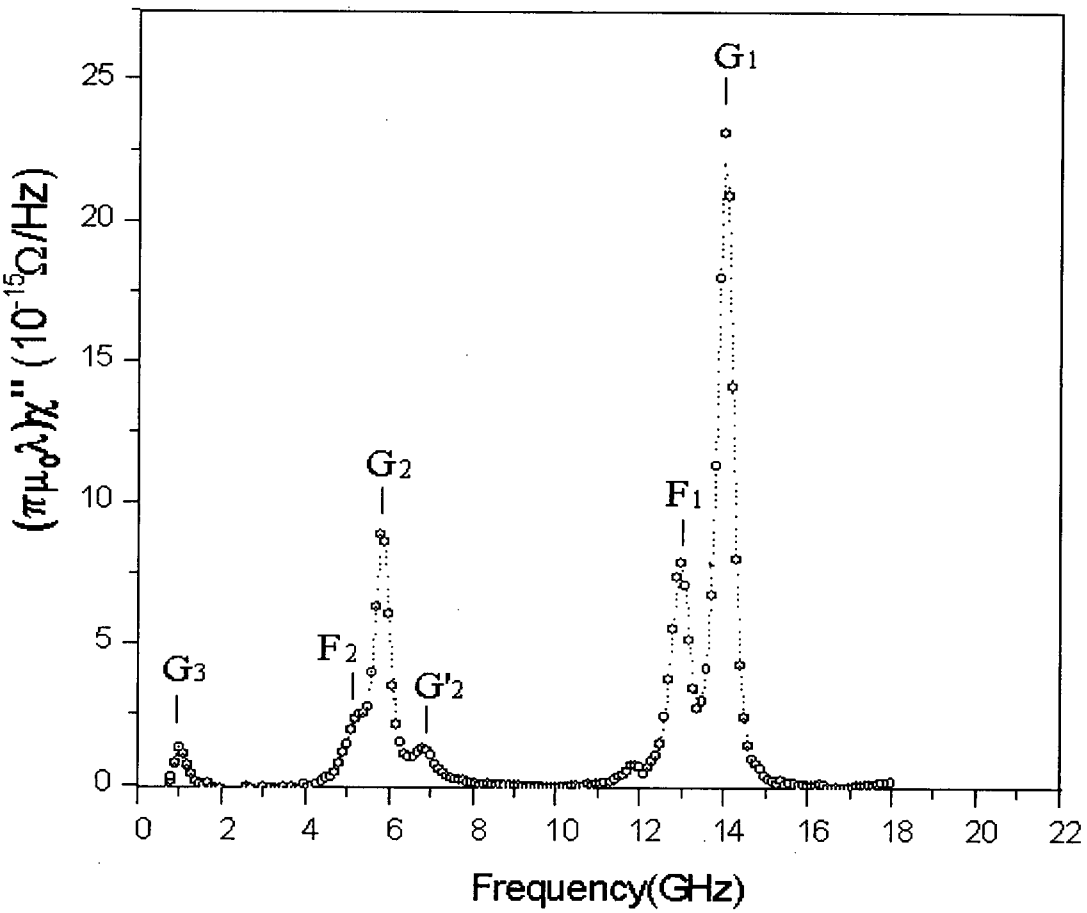

Figure 7.2: The magnetic susceptibility χ'' of $Gd_{0.01}Y_{0.99}Ba_2Cu_3O_{6.92}$ up to a factor of $\pi\mu_0\lambda$ obtained from the surface resistance measurement by subtracting the background (R_s^{SC}) and dividing by the frequency.

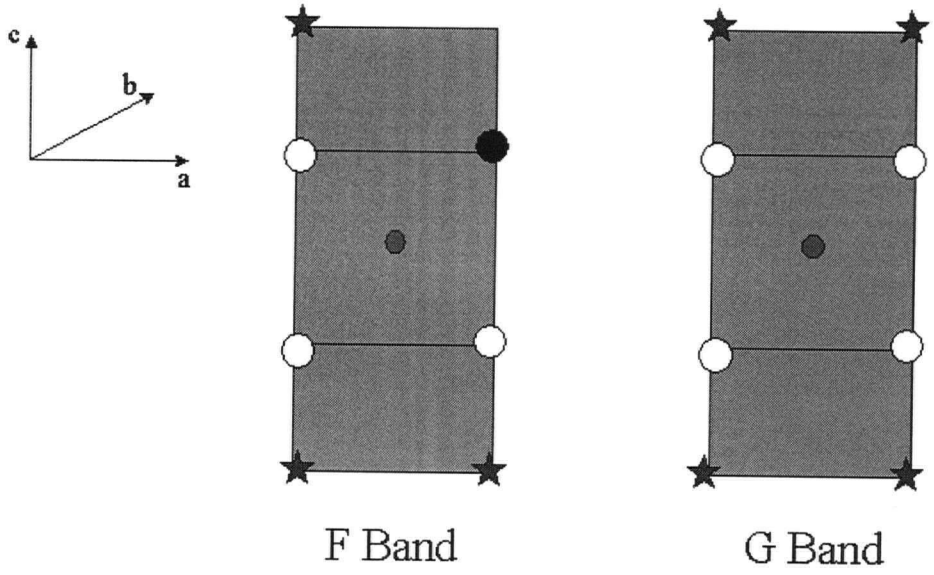

Figure 7.3: Two different CF environments. The Gd ion may have four (G-band) or three (F-band) nearest neighbour chains. The stars represent a chain, open circles are holes in the Cu-O plane and the black circle represents a missing hole (electron)

7.1.1 Oxygen Ordering

Research by Rockenbauer *et al.* [24, 27] has shown that such a spectrum should be fitted by two sets of CF parameters. At an oxygen doping of 6.92 the Cu-O chains along the $\hat{b}$ axis are not completely full. As a consequence, some Gd sites have four nearest neighbour chains and some have less. At this oxygen content, 8% of the chain oxygens are missing and approximately 32% of the Gd sites have only three nearest neighbour chains (neglecting the sites with two and less chains). The other 68% of Gd sites have four nearest neighbour chains. This results in two different CF environments for the two different Gd sites as shown in figure 7.3. We will denote the spectrum of the ions with four nearest neighbour chains as the G-band and the spectrum of the ions with three nearest chains as the F-band. The spectrum of the optimally doped sample (shown in figure 7.2) was fitted with two sets of CF parameters. The first guesses were taken from the work of Rockenbauer *et al.* on $Y_{0.999}Gd_{0.001}Ba_2Cu_3O_{6.77}$ [24], and some adjustments were made to fit our data (see the fitting procedure in chapter 6). The two sets are presented in table 7.1 with the CF parameters of ref. [24]. The transitions were identified as summarized in table 7.2 and the fitted data is shown in figure 7.4. In this case, the function $\chi''(\omega)$ is a

sum of the two bands:

$$\chi''(\omega) = \frac{1}{1+r}(\chi''_G(\omega) + r\chi''_F(\omega)) \tag{7.1}$$

where r is the weight of the F band, relative to the G band. In the spectrum, r can be extracted from the relative intensities of two peaks that represent the same transition in the different bands. The Hamiltonian of spins with four nearest neighbour chains is described by the G-band CF parameters and therefore, these spins will contribute to the intensity of the G_i transitions. In the same way, the intensities of the F_i transitions are proportional to the number of spins in the F band:

$$\frac{A^F_{NJ}}{A^G_{NJ}} = \frac{N^F_j - N^F_i}{N^G_j - N^G_i} = r(e^{-\beta E^F_j} - e^{-\beta E^F_i})/(e^{-\beta E^G_j} - e^{-\beta E^G_i}) \tag{7.2}$$

where A^F_{ij} is the integrated intensity of the $i \rightarrow j$ transition in the F-band and E^F_i is the ith energy level in the F band and $\beta = 1/k_B T$. This ratio is directly related to the oxygen content of the crystal:

$$1 - \delta = \frac{4+3r}{4(1+r)}. \tag{7.3}$$

Using the integrated intensities of the two largest transitions in the optimally doped sample's spectrum (which correspond to the $\pm\frac{5}{2} \rightarrow \pm\frac{7}{2}$ in the G and F bands) gives an oxygen content of 6.94, in reasonably good agreement with the expected content of 6.92, from the knowledge of the annealing temperature and pressure.

	B^0_2	B^2_2	B^0_4	B^4_4	B^0_6
G-band	-590 (-598)	0 (0)	-3.1 (-3.1)	12.7 (13.2)	0.167 (0.167)
F-band	-533 (-541)	0 (0)	-3.1 (-3.1)	12.5 (17.2)	0.167 (0.158)
r, F:G Ratio	0.34				

Table 7.1: Crystal field parameters for the two ESR bands in an optimally doped YBCO, given in GHz. In brackets - the CF parameters as measured by Rockenbauer *et al.* in conventional ESR on a powder sample of $Y_{0.999}Gd_{0.001}Ba_2Cu_3O_{6.77}$ [24].

The extracted penetration depth from this fitting is $1270\mathring{A}$ and since the crystal is twinned, this is a weighted average between λ_a and λ_b. Another contribution to this extracted penetration depth comes from λ_c. The correction is discussed in section 7.3.

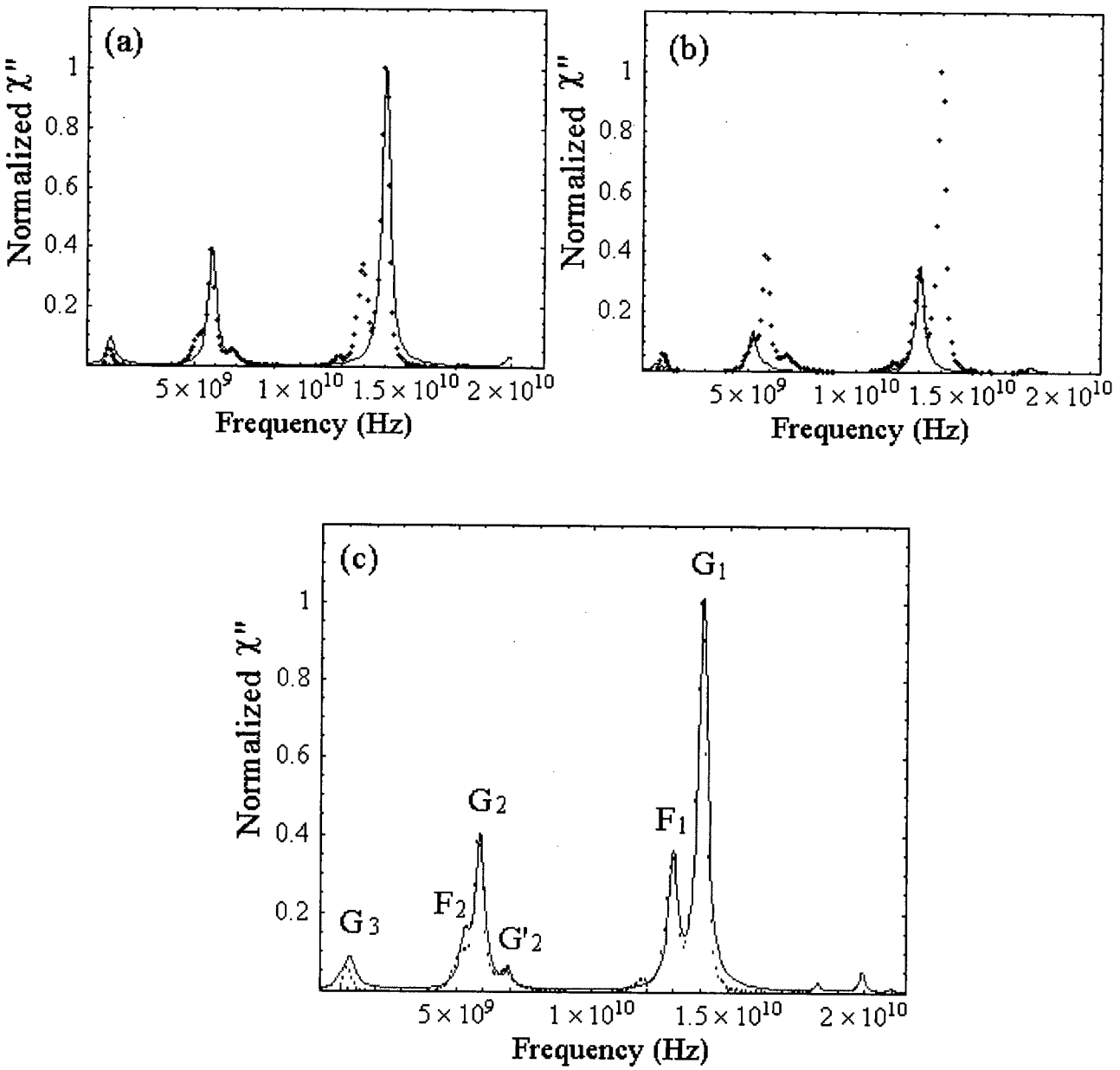

Figure 7.4: The fitted ESR spectrum of an optimally doped YBCO sample with 1.28% Gd. The spectrum is a superposition of two bands. Figure (a) shows The G-band fitting, figure (b) shows the F-band fitting and figure (c) shows the sum. The dots are experimental data points and the line is the theoretical spectrum generated by the Mathematical program.

Label	Frequency (GHz)	Transition
G_1	14.04	$\pm 5/2 \rightarrow \pm 7/2$
G_2	5.86	$\pm 3/2 \rightarrow \pm 5/2$
G_2'	6.90	$\pm 1/2 \rightarrow \pm 5/2$
G_3	1.05	$\pm 1/2 \rightarrow \pm 3/2$
F_1	13.02	$\pm 5/2 \rightarrow \pm 7/2$
F_2	5.20	$\pm 3/2 \rightarrow \pm 5/2$

Table 7.2: ESR Transitions in a twinned optimally doped YBCO sample. Transitions of the G-band are labeled G_i and F-band transitions are labeled F_i

7.2 Detwinned Overdoped Crystal

In order to verify the two band theory another measurement was performed on a $Gd_{0.0128}Y_{0.972}Ba_2Cu_3O_{6.99}$ sample. To further simplify matters, this sample was detwinned. This oxygen content was chosen in order to achieve a spectrum containing predominantly one band, the G-band. At this doping, the chains along the $\hat{b}$ axis are almost completely full, we expect a ratio of 1:0.04 between the two peaks observed earlier. Figure 7.5 shows that our expectations were verified and the spectrum contains only three main peaks with only a small contribution of the F_1 transition, while the other F-band transitions are not visible.

Another interesting feature of the data is the difference in spectra between the two directions. This crystal was detwinned and therefore we can use this data to separate the measurements of λ_a and λ_b. The spectra show a difference in the intensity as a result of the different penetration depths in the $\hat{a}$ and $\hat{b}$ directions. In addition, the shape of the spectrum in the two directions is different. The $\hat{a}$ direction spectrum has three main peaks and in the $\hat{b}$ direction we see four main lines. The additional line (marked as G_2') is the result of an off diagonal transition, $\pm\frac{1}{2} \rightarrow \pm\frac{5}{2}$. Such a direction sensitive feature can only result from an operator that violates the $\frac{\pi}{2}$ rotational symmetry in the x-y (a-b) plane. Operators of this type are the result of the crystal's orthorhombicity and the relevant operators are: O_2^2, O_4^2 and O_6^2. The dominant contribution is of course the first orthorhombic term in the expansion: $O_2^2 = \frac{1}{2}(S_+^2 + S_-^2) = \frac{1}{2}(S_x^2 - S_y^2)$. The coefficient B_2^2 of this operator was adjusted (using a Mathematica simulation) to simultaneously fit the data in both directions. This transition was also visible in the optimally doped crystal but since the sample was twinned, the orthorhombic nature was not resolved. The determination of the CF parameter B_2^2 can therefore only be done on detwinned samples. The crystal field parameters are given in table 7.3 and the identified transitions are given in table 7.4.

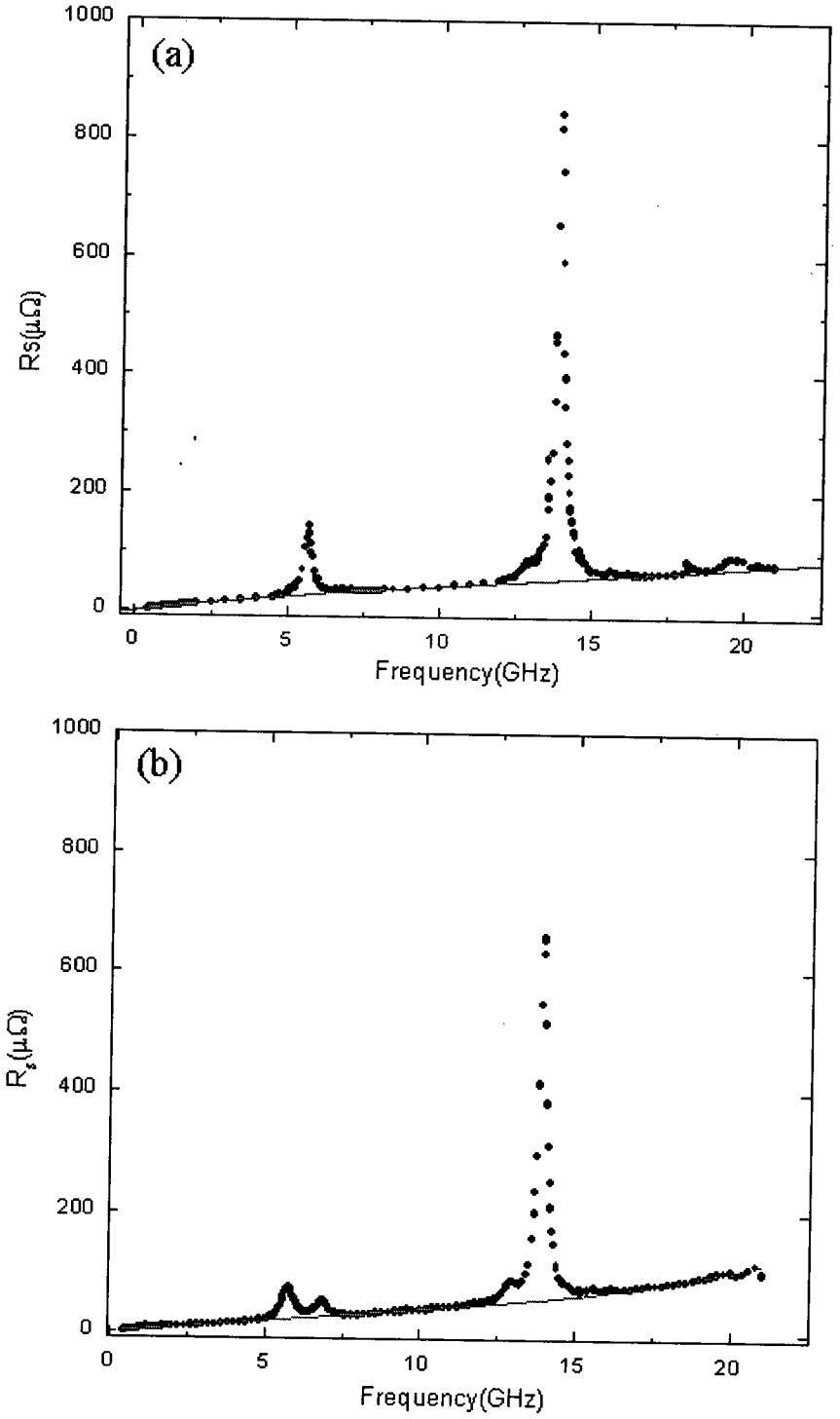

Figure 7.5: Surface resistance of an over doped YBCO sample with 1.28% Gd. Figure (a) shows the spectrum of the $\hat{a}$ direction and figure (b) shows the $\hat{b}$ direction. In both figures the measured surface resistance is shown (dots) along with a polynomial fit to the background (line)

The data with the theoretical fit for the $\hat{a}$ and $\hat{b}$ directions are shown in figure 7.6.

	B_2^0	B_2^2	B_4^0	B_4^4	B_6^0
G-band	-583 (-598)	26.7 (0)	-3.1 (-3.1)	12.7 (13.2)	0.167 (0.167)
F-band	-530 (-541)	0 (0)	-3.1 (-3.1)	12.8 (17.2)	0.159 (0.158)
r, F:G Ratio	0.04				

Table 7.3: Crystal field parameters for the ESR spectrum in an overdoped YBCO crystal, given in GHz. In brackets - the CF parameters as measured by Rockenbauer *et al.* in conventional ESR on a powder sample of $Y_{0.999}Gd_{0.001}Ba_2Cu_3O_{6.77}$ [24].

Label	Frequency (GHz)	Transition
G_1	14.04	$\pm 5/2 \rightarrow \pm 7/2$
G_2	5.86	$\pm 3/2 \rightarrow \pm 5/2$
G_2'	6.90	$\pm 1/2 \rightarrow \pm 5/2$
G_3	1.05	$\pm 1/2 \rightarrow \pm 3/2$
F_1	13.02	$\pm 5/2 \rightarrow \pm 7/2$
F_2	5.20	$\pm 3/2 \rightarrow \pm 5/2$

Table 7.4: ESR Transitions in a detwinned overdoped YBCO sample. Both the a and b spectra show the same transitions except for the G_2' transition that is only visible in the b direction

7.3 Corrections for $\hat{c}$ Axis Currents

Corrections to the above figures should be made because of c-axis contributions to the effective penetration depth. In our experiment the magnetic field is applied along the $\hat{b}$ ($\hat{a}$) direction and the currents flow mainly in the a-b plane. However, a small portion of the current flows in the b-c plane, along the $\hat{c}$ direction. As a result the measured penetration depth, λ_{eff}, is a mixture of the in plane penetration depth, λ_a (λ_b), and λ_c. A method used for separating the two contributions was employed at the UBC superconductivity lab [26, 32] in overdoped YBCO crystals ($x = 0.95 - 0.99$). This technique involves a cavity perturbation measurement of R_s. The sample is then cleaved into 2 or 3 long platelets along the $\hat{b}$ ($\hat{a}$) direction and R_s is measured again. The increase in the observed surface resistance can be attributed to the additional b-c planes in the platelets and therefore to the $\hat{c}$ axis transport.

In the case of Gd doped crystals, this measurement has not been done yet and the corrections given here are based on previous measurements of the $\hat{c}$ penetration depth.

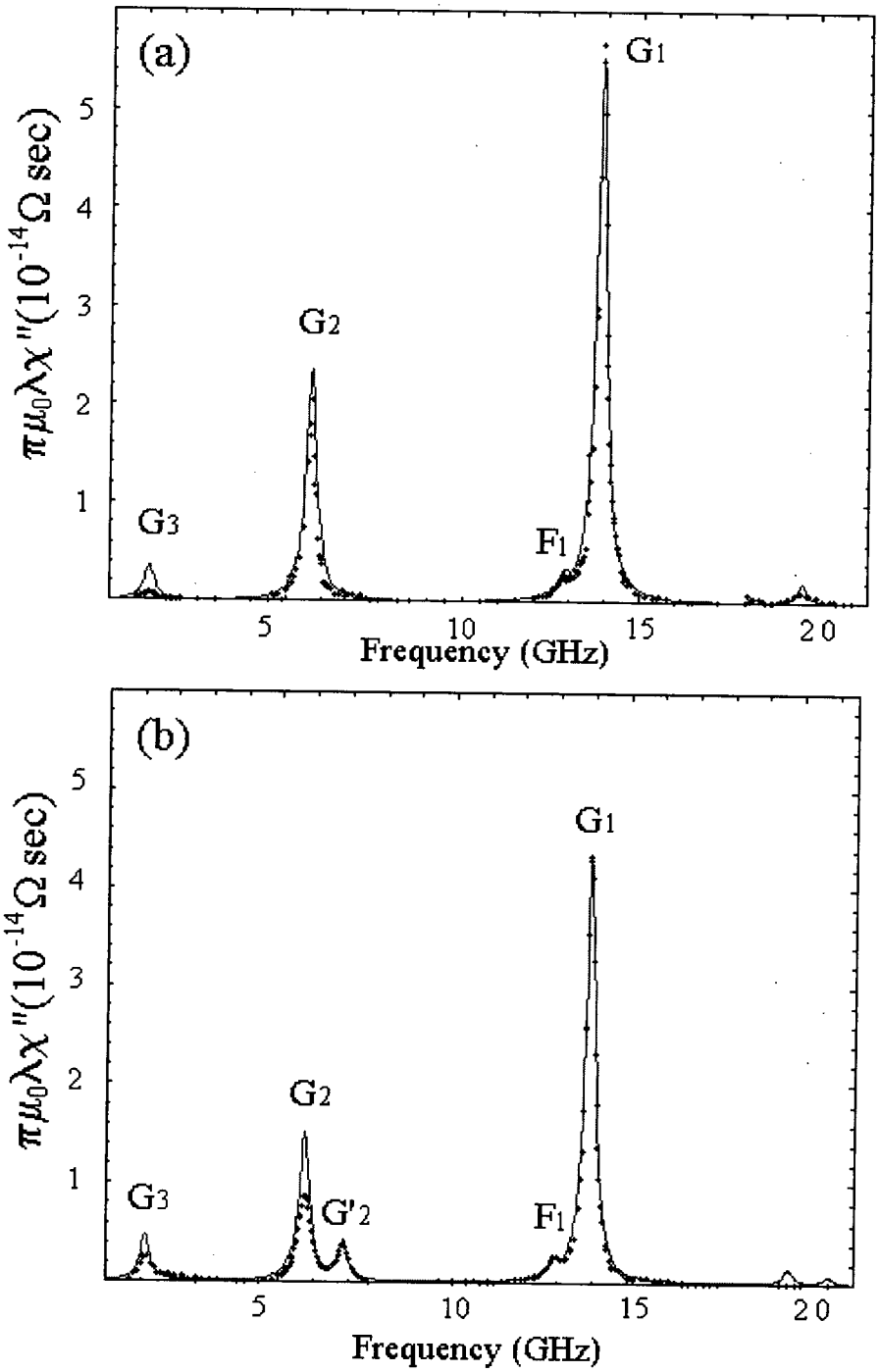

Figure 7.6: The fitted ESR spectrum of an over doped YBCO sample with 1.28% Gd. The spectrum has essentially only one ESR band, the G-band. Figure (a) shows the spectrum of the $\hat{a}$ direction, where the currents are running in the $\hat{a}$ direction and the magnetic field is applied along the $\hat{b}$ direction. Figure (b) shows the $\hat{b}$ direction, where the middle main line is split into two peaks by the O_2^2 crystal field operator. The dots are experimental data points and the line is the theoretical spectrum generated by our Mathematica simulation.

We used the value of $\lambda_c = 11,000 \pm 400\mathring{A}$ that was measured in $YBa_2Cu_3O_{6.99}$ at $1.2K$ [32]. The first, twinned sample had dimensions of $x = 820\mu m$ and $c = 19\mu m$ where x is the length of the sample along the measured direction. The second, detwinned sample has dimensions of $a = 770\mu m$, $b = 910\mu m$ and $c = 23\mu m$.

A simple, straightforward correction assumes that the Gd ions that are exposed to the field near the b-c plane are in a volume of $2 \times a \times b \times \lambda_c$:

$$\lambda_{eff} = \frac{a\lambda_a + c\lambda_c}{a}. \tag{7.4}$$

A more accurate calculation([33]) of a field profile in a sample of rectangular cross section uses the anisotropic screening equation:

$$\lambda_c^2 \frac{\partial^2 H}{\partial z^2} + \lambda_a^2 \frac{\partial^2 H}{\partial x^2} = H. \tag{7.5}$$

The solution to this equation is:

$$\lambda_{eff} = \frac{ac}{a+c}\frac{4}{\pi^2} \sum_{odd\ n>0} \frac{1}{n^2} \left\{ \frac{tanh(\alpha_n)}{\alpha_n} + \frac{tanh(\beta_n)}{\beta_n} \right\} \tag{7.6}$$

$$\text{with } \alpha_n = \frac{c}{2\lambda_a} \left[1 + \left(\frac{n\pi\lambda_c}{a} \right)^2 \right]^{\frac{1}{2}} \tag{7.7}$$

$$\beta_n = \frac{a}{2\lambda_c} \left[1 + \left(\frac{n\pi\lambda_a}{c} \right)^2 \right]^{\frac{1}{2}} \tag{7.8}$$

Table 7.5 summarize the results for λ_{plane} of the twinned crystal and λ_a and λ_b for the detwinned crystal and their corrections in the two methods.

	extracted $\lambda(\mathring{A})$	simple $\hat{c}$ correction	full calculation
λ_{plane}, twinned sample	1270 ± 130	1019 ± 140	1025 ± 140
λ_a, detwinned sample	1684 ± 175	1355 ± 187	1410 ± 187
λ_b, detwinned sample	1347 ± 140	1069 ± 150	1100 ± 150

Table 7.5: The ESR-extracted penetration depth λ of an optimally doped twinned sample and an overdoped detwinned sample, at $T = 1K$. Both samples have 1.28% Gd concentration.

7.4 Error analysis

Errors in the extracted λ come from both experimental errors and the function fitting procedure. The experimental errors in the bolometric apparatus are estimated as 5-10% in the raw R_s data [19]. Another source of error is the Gadolinium concentration in the crystal that is estimated to be $1.28 \pm 0.02\%$. In the fitting procedure there are two sources of error, the first is the background subtraction in which we fit a polynomial function to the data between ESR peaks. This fitting is quite accurate away from the peaks and only affects the tail of the Lorentzians. After the background R_s^{SC} is subtracted, the data is divided by the frequency to give a quantity proportional to χ''. For the small peak the background fitting inaccuracy is enhanced by a large factor of order $\frac{1}{\omega}$ since the frequency is low and the actual line intensity may be changed by up to 50%. However, for the largest peak the background subtraction error is small compared to the intensity of the line and is divided by a large factor since the frequency is high. The best fit parameter λ is chosen to fit the largest transition and therefore we neglected the background subtraction error. The second fitting error is the actual curve fitting of the theoretical data (a sum of Lorentzians) to the experimental data. An estimation of this error is given by Origin (the data analysis program) as the errors of the fitted Lorentzian area. This error is estimated to be less then 2%. The errors mentioned above are uncorrelated and therefore add in the following way:

$$\left(\frac{\delta\lambda_L}{\lambda_L}\right)^2 = \left(\frac{\delta R_s}{R_s}\right)^2 + \left(\frac{\delta N_{Gd}}{N_{Gd}}\right)^2 + \left(\frac{\delta A}{A}\right)^2 \tag{7.9}$$

where N_{Gd} is the gadolinium concentration, R_s is the surface resistance and A is the intensity of the largest ESR transition that is used to fit λ. This leads to the following relative error in λ_L (before $\hat{c}$ axis correction):

$$\left(\frac{\delta\lambda_L}{\lambda_L}\right) = \sqrt{(10\%)^2 + (2\%)^2 + (2\%)^2} = 10.4\% \tag{7.10}$$

Another error comes from the λ_c value that is used for the $\hat{c}$ axis correction. We can calculate the error of the corrected λ_a (or λ_b) using the simple formula for the $\hat{c}$ axis correction:

$$\lambda_a = \lambda_{eff} - \frac{c}{a}\lambda_c \tag{7.11}$$

where the error in λ_{eff} was calculated in the previous paragraph and $\lambda_c = 11,000 \pm$

$400\mathring{A}$. The total error in λ is then given by:

$$\delta\lambda = \delta\lambda_{eff} + \frac{c}{a}\delta\lambda_c. \tag{7.12}$$

The errors for each value of λ are given in table 7.5.

8: Conclusions

The main goal of this work was to develop a reliable method for measuring the absolute value of the low temperature limit of the magnetic penetration depth, $\lambda_L(T \to 0)$. This goal was convincingly achieved through a surprising and unconventional combination of two experimental methods, ESR and broad band microwave surface resistance measurements. The new technique was applied to YBCO crystals and the results that were obtained are in reasonable agreement with μSR [8, 9] and infrared [10] measurements.

However, there are still some open issues regarding the reliability and the errors of the figures given. Most concerning is the difference between our measured λ_a, λ_b of the overdoped detwinned sample and λ_{plane} of the optimally doped twinned crystal. We expected λ_{plane} to be intermediate to the values of λ_a and λ_b (when measured in the same sample) since it is a weighted average of the two directions. In practice, λ_{plane} was found to be smaller then both λ_a and λ_b. This may indicate a change in penetration depth due to the different superfluid density but may also be the result of a difference in Gd concentration between the two samples. The later possibility is currently being checked out.

Several directions of study are possible for further work. Performing a series of measurements on YBCO with different oxygen contents will provide information on the dependence of the superfluid density and the crystal field parameters on doping. The results can then be combined with T_c measurements of the same samples and presented as a Uemura plot [3] (when we plot T_c vs. $1/\lambda^2$) to verify the dependence of T_c on superfluid density. Another product of this series of measurements would be the CF parameters for each doping. This would complement the work of Rockenbauer *et al.* [24] in single crystals (rather than aligned powder) and extend it to higher doping levels.

Another useful measurement that can be done with the existing samples is the $\hat{c}$-axis penetration depth λ_c. This can be done by cleaving the sample as described in reference [26]. This measurement will provide, in addition to the value of λ_c, the appropriate $\hat{c}$-axis correction to our $\lambda_{a/b}$.

However, by far the most significant result of the success of this method is that it allows us to measure λ absolutely, on crystals that are essentially identical to the

crystals used in the lab's surface resistance measurements. In turns this allows us to extract the microwave conductivity σ_1 from the surface resistance values. In the past all of our conductivity values have had relatively large uncertainties because of uncertainties in λ.

It may also be possible to use the same measurement principle in other superconductors. The feasibility of the technique depends on finding the right atomic substitution and knowing the fine structure of the ion at the relevant crystal site, at least to first order. Knowing the CF parameters, one can then calculate the frequencies of the various transitions and design an experiment to cover the relevant range.

As described in chapter 5, the experiments were done in a bolometric apparatus [19]. Further development of the bolometric experiment is under way. The frequency range will be extended to higher frequencies (up to 50GHz) and to lower temperatures (down to 100mK). With these experimental improvements we will be able to measure λ_L closer to the limit of zero temperature, and the broader band of frequencies may become useful in measurements of other materials.

References

[1] J. Bardeen, L. N. Cooper, and J. R. Schriffer. Theory of superconductivity. *Physical Review*, 108:1175–1204, December 1957.

[2] W. N. Hardy, D. A. Bonn, D.C. Morgan, Ruixing Liang, and Kuan Zhang. Precision measurement of the temperature dependence of λ in $YBa_2Cu_3O_{6.95}$: Strong evidence for nodes in the gap function. *Physical Review Letters*, 70(25):3999–4002, June 1993.

[3] Y. J. Uemura, G. M. Luke, B. J. Sterlieb, J. H. Brewer, J. F. Carolan, W. N. Hardy, R. Kadono, J. R. Kempton, R. F. Kiefl, S. R. Kreitzman, P. Mulhern, T. M. Riseman, D. Li. Wlilams, B. X. Yang, S. Uchida, H. Takagi, J. Gopalakrishnan, A. W. Sleight, M. A. Subramanian, C. L. Chien, M. Z. Ciepalk, Gang Xiao, V. Y. Lee, B. W. Statt, C. E. Stronach, W. J. Kossler, and X. H. Yu. Universal correlation between t_c and $n_s/m*$ (carrier density over effective mass) in high-t_c cuprate superconductors. *Physical Review Letters*, 62(19):2317–2320, May 1989.

[4] A. Hosseini, R. Harris, Saeid Kamal, P. Dosanjh, J. Preston, Ruixing Liang, W. N. Hardy, and D.A. Bonn. Microwave spectroscopy of thermally excited quasiparticles in $YBa_2Cu_3O_{6.99}$. *Physical Review B*, 60(2):1349–1359, July 1999.

[5] S. Kamal, Ruixing Liang, A. Hosseini, D.A. Bonn, and W. N.Hardy. Magnetic penetration depth and surface resistance in ultrahigh-purity $YBa_2Cu_3O_{7-\delta}$ crystals. *Physical Review B*, 58(14):R8933–R8936, October 1998.

[6] S. Kamal, D.A. Bonn, Nigel Goldenfeld, P.J. Hirschfeld, Ruixing Liang, and W. N.Hardy. Penetration depth measurements of 3d xy critical behavior in $YBa_2Cu_3O_{6.95}$ crystals. *Physical Review Letters*, 73(13):1845–1848, September 1994.

[7] D. A. Bonn and W. N. Hardy. Microwave surface impedance of high temperature superconductors. In Donald M. Ginsberg, editor, *Physical Properties of High*

Temperature Superconductors, volume V, chapter 2, pages 7–98. World Scientific, 1995.

[8] Jeff E. Sonier, Jess H. Brewer, and Robert F. Kiefl. μsr studies of the vortex state in type-ii superconductors. *Reviews of modern physics*, 72(3):769–807, July 2000.

[9] J. L. Tallon, C. Bernhard, U. Binninger, A. Hofer, G. V. M. Williams, E. J. Ansaldo, J. I. Budnick, and Ch. Niedermayer. In-plane anisoropy of penetration depth due to superconductivity of cu-o chains in $YBa_2Cu_3O_{7-\delta}$, $Y_2Ba_4Cu_7O_{15-\delta}$, and $YBa_2Cu_4O_8$. *Physical review letters*, 74(6):1008–1011, February 1995.

[10] D.N. Basov, R.Liang, D.A. Bonn, W.N. Hardy, B. Dabrowski, M. Quijada, D.B Tanner, J.P. Rice, D.M. Ginsberg, and T. Timusk. In-plane anisoropy of the penetration depth in $YBa_2Cu_3O_{7-x}$ and $YBa_2Cu_4O_8$ superconductors. *Physical review letters*, 74(4):598–601, January 1995.

[11] M. Tinkham. *Superconductivity.* Gordon and Breach, science publishers, 1965.

[12] D. A. Bonn and W. N. Hardy. Microwave properties of high temperature superconductors. *Physics in Canada*, 56(5):243–246, September/October 2000.

[13] John David Jackson. *Classical Electrodynamics.* John Wiely & Sons, Inc., 3rd edition, 1998.

[14] P. G. De Gennes. *Superconductivity of Metals and Alloys.* advanced book program. Persus books, 1999.

[15] J. S. Griffith. *The Theory of Transition Metal Ions.* The Camridge University Press, 1961.

[16] K.W.H. Stevens. *Magnetic Ions in Crystals.* Princeton university press, 1997.

[17] A. Abargam and B. Bleaney. *Electron Paramagnetic Resonance of Transition Ions.* Clarendon press - Oxford, 1970.

[18] M. Divis and V. Nekvasil. Semi-empirical and ab-initio calculations of the crystal field interactions in rare earth cuprates. *Journal of Alloys and Compaunds*, 1, 2001.

[19] Patrick J. Turner. A bolometric technique for broadband measurement of suface resistance and application to single crystal $YBa_2Cu_3O_{6.99}$. Master's thesis, The University of British Columbia, October 1999.

[20] D. Shaltiel, S.E. Barnes, H. Bill, M. Francois, H. Hagemann, J. Jegondaz, D. Lovy, P. Monod, M. Peter, A. Revcolevschi, W. Sadowaski, and E. Walker. Unusual behavior of gd esr in single crystals of $Gd_yY_{1-y}Ba_2Cu_3O_{6+x}$ with $x = 0.1 - 0.8$ and $y = 0.03 - 0.06$: Evidence for a magnetic interaction in the superconductors. *Physica C*, 161:13–20, August 1989.

[21] A Janossy, A. Rockenbauer, and S. Pekker. Gd^{3+} electron paramagnetic resonance in the quazi-two-domentional antiferromagnet $YBa_2Cu_3O_{6+y}$: Gd. *Physica C*, 167:301–306, 1990.

[22] A Janossy, A. Rockenbauer, S. Pekker, G. Oszlanyi, G. Faigel, and L. Korecz. Epr in gd-doped $YBa_2Cu_3O_{6+y}$: local method to determine oxygen ordering. *Physica C*, 171:457–464, 1990.

[23] A Janossy, L.-C. Brunel, and J. R. Cooper. Gd^{3+} esr determination of the spin susceptibility in Gd : $YBa_2Cu_3O_{6+y}$ high-temperature superconductors. *Physical review B*, 54(14):10 186 - 10 191, 1996.

[24] A. Rockenbauer, A. Janossy, L. Krecz, and S. Pekker. Electron paramagnetic resonance spectroscopy of gd doped $YBa_2Cu_3O_{6+x}$ in a magnetic field. *Journal of Magnetic Resonance*, 97:540–552, August 1992.

[25] S. Sridhar and W. L. Kennedy. Novel technique to measure the microwave response of high t_c between 4.2 and 200k. *Review of scientific instruments*, 59(4):531–536, April 1988.

[26] A. Hosseini, Saeid Kamal, D.A. Bonn, Ruixing Liang, and W.N. Hardy. $\hat{c}$-axis electrodynamics of $YBa_2Cu_3O_{\delta-7}$. *Physical review letters*, 81:1298–1301, March 1998.

[27] S. Pekker, A. Janossy, and A. Rockenbauer. Ordering of oxygen into chains and distribution of hole density in $YBa_2Cu_3O_{6+x}$. *Physica C*, 181:11–17, 1991.

[28] Ruixing Liang, D.A Bonn, and W.N. Hardy. Perfecting the growth of ybco crystals. *Physics in Canada*, 56(5):243–246, September/October 2000.

[29] Ruixing Liang, D.A. Bonn, and Walter N. Hardy. Preparation and x-ray characterization of highly ordered ortho-ii phase $YBa_2Cu_3O_{6.5}$ single crystals. *Physica C*, 336:57–62, 2000.

[30] P. Schleger, W.N. Hardy, and B.X. Yang. Thermodynamics of oxygen in $Y_1Ba_2Cu_3O_x$. *Physica C*, 176:261–273, 1991.

[31] Charles Kittel. *Introduction to Solid State Physics.* John Wiely & Sons, Inc., 6th edition, 1986.

[32] C.C. Homes, S. Kamal, D.A. Bonn, R. Liang, W.N. Hardy, and B.P.Clayman. Determination of the condensate from optical techniques in unconventional superconductors. *Physica C*, 296:230–240, 1998.

[33] David Broun. *The Microwave Electrodynamics of Unconventional Superconductors.* PhD thesis, Pembroke College, Cambridge, January 2000.

A: Cavity Perturbation Technique

Cavity perturbation is a particularly useful tool for measuring the microwave electrodynamics of small single crystals of high T_c superconductors. This appendix explains the basic idea of cavity perturbation technique.

In general a resonance cavity has a complex eigen frequency that is composed of the frequency ω (the real part) and the inverse quality factor Q (the imaginary part).

$$\tilde{\omega} = \omega(1 + \frac{i}{2Q}) \tag{A.1}$$

In an empty cavity the resonance frequency is a function of the cavity's geometry and the quality factor is a function of the losses in the cavity walls. When a sample (metal or superconductor) is inserted into the cavity the resonance frequency changes. The change is due to the new boundary conditions for the electromagnetic fields and resulting new field configuration as well as the loss on the sample's surface (the sample's surface resistance).

In order to measure the temperature dependence of the sample's surface impedance the following steps are taken. The losses in the cavity walls are kept constant throughout the experiment, so that any change in Q is caused by a change in the sample's surface resistance. This is done by keeping the cavity at a constant base temperature and heating only the sample above this temperature. The field configuration in the cavity should be constant so that the changes in the resonance frequency would only be due to the change in the sample's penetration depth. This is done by keeping the sample at one place and working at a resonance frequency that is well separated from other resonances. When the above steps are taken, the changes in $\tilde{\omega}$ are only a function of the changes in the sample's surface impedance. The extraction of the sample's surface impedance is based on the relation:

$$\Delta\tilde{\omega} \propto i \int_{sample} \Delta Z_s J_s^2. \tag{A.2}$$

The integrated surface current is assumed to be unchanged and therefore the change

in surface impedance can be resolved:

$$\Delta\tilde{\omega} = \Delta\omega + i\Delta\frac{1}{2Q} = iK\Delta Z_s = iK\Delta R_s - K\Delta X_s. \tag{A.3}$$

The proportionality constant K is a function of the cavity and sample geometry and can be calculated for simple geometries or measured using a reference sample with known properties and similar dimensions.

Achieving the absolute surface impedance of the sample in this way is not trivial. The relevant origin of the complex frequency, $\tilde{\omega}_0$, is of the cavity with a sample of no surface resistance and zero penetration depth. This limit is of course not accessible by experiment. The measured Q of the cavity without the sample can be taken as a good zero point for the surface resistance R_s since then the sample's contribution to the loss is zero. For the surface reactance, this does not work since the origin of X_s is a sample with zero penetration depth (acavity with no sample is the opposite situation). In this approach (taken by our group) one can only measure ΔX_s.

Another approach is to use the fact that at the normal state $R_s = X_s$ [?]. The frequency origin is set in the normal state and the $\frac{1}{Q}$ origin is set well in the superconducting state where the loss is orders of magnitude smaller. This method yields an absolute measurement of Z_s but has large uncertainties.

B: Surface Current in a Uniform magnetic Field

This appendix explains equation 5.2 of chapter 5:

$$\frac{P^{sample}}{P^{reference}} = \frac{R_s^{sample}}{R_s^{reference}} \tag{B.1}$$

where the reference and sample experience the same magnetic field H.

As discussed in chapter 3, the classical skin effect leads to an exponential decay of AC magnetic fields into the sample. In a normal metal this decay is proportional to $e^{i(1+i)r/\delta}$ where δ is the skin depth and in a superconductor the decay is proportional to $e^{-r/\lambda}$ where λ is the magnetic penetration depth. In both cases the magnetic field deep inside the sample is essentially zero and the currents flow on the surface within the small penetration depth or skin depth. This results in a surface current, J_s, (the current density integrated over the thickness λ or δ) that is equal to the applied magnetic field.

To obtain this consider the geometry described in figure B.1 where the magnetic field, $\vec{H}$, is applied parallel to the crystal's $\hat{a}$ axis and the currents are flowing in the a-b and a-c planes perpendicular to the $\hat{a}$ direction. Now let us integrate Ampere's law, $\vec{\nabla} \times \vec{H} = \vec{J}$, over the rectangular surface S that is parallel the a-c plane and has an edge l (see figure B.1). The upper edge of S lays on the upper a-b plane, where the supercurrent is flowing, and the lower edge is well inside the sample where both the magnetic field and the current are zero. The integration gives:

$$\int (\vec{\nabla} \times \vec{H}) \cdot d\vec{S} = \int \vec{J} \cdot d\vec{S} = J_s \cdot l \tag{B.2}$$

where the last equality is consistent with our definition of the surface current per unit width (in this case the current is flowing mainly in the $\hat{b}$ direction and the width is along the $\hat{a}$ direction). Using Stokes theorem we can simplify the left hand side of the equation:

$$\int (\vec{\nabla} \times \vec{H}) \cdot d\vec{S} = \oint_{\partial S} \vec{H} \cdot d\vec{l} \tag{B.3}$$

where $d\vec{l}$ runs over the contour of the surface S. Since $\vec{H}$ is applied in the $\hat{a}$ direction and is zero in the middle of the sample, the only contribution to this integral is from

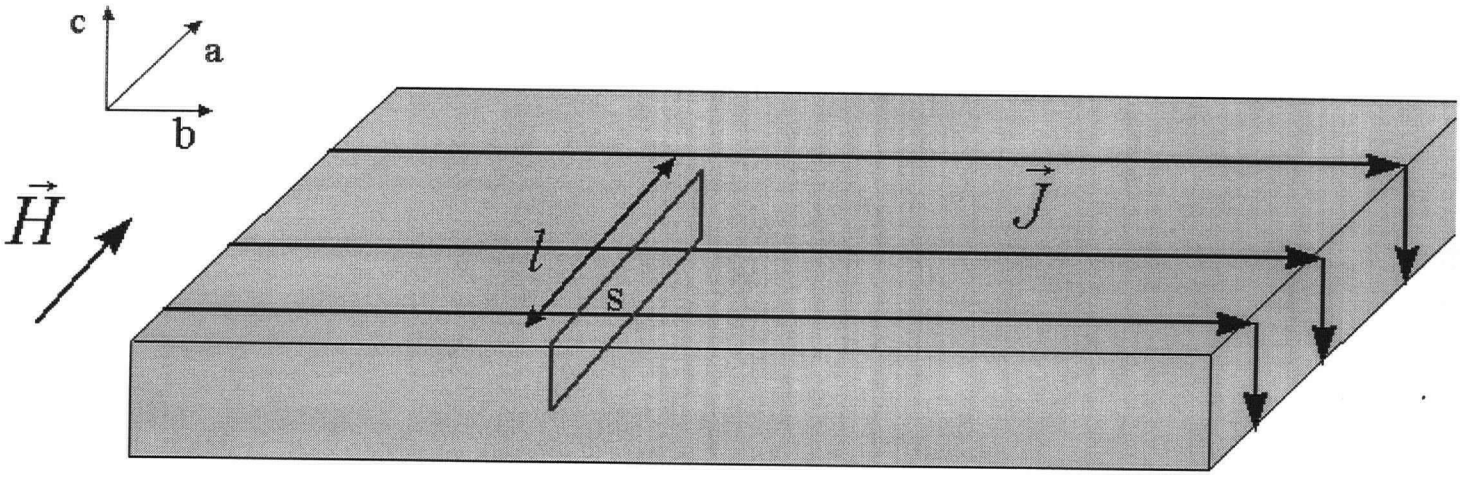

Figure B.1: A typical high T_c sample in a magnetic field. The magnetic rf field is applied along the $\hat{a}$ direction the current is flowing mainly in the $a-b$ plane along the $\hat{b}$ direction. The field and current deep inside the sample are zero.

the part of the contour along the sample's surface (in the $\hat{a}$ direction) and therefore:

$$H_a \cdot l = J_s \cdot l \Rightarrow H_a = J_s. \tag{B.4}$$

With this result we can now calculate the ratio of absorbed power in the sample and reference. The power absorption of a sample per unit area in an rf magnetic field is given by

$$P_{sample} = \frac{1}{2} R_s J_s^2 = \frac{1}{2} R_s H^2 \tag{B.5}$$

where R_s is the surface resistance and J_s is the current density. Since the two samples experience the same magnetic field, result B.1 follows.